J. Fluid Mech. (2014), *vol.* 749, *pp.* 367–403. © Cambridge University Press 2014
doi:10.1017/jfm.2014.225

Turbulent drag reduction of boundary layer flow with non-ionic surfactant injection

Shinji Tamano†, Takuya Kitao and Yohei Morinishi

Graduate School of Engineering, Nagoya Institute of Technology, Gokiso-cho, Showa-ku, Nagoya, Aichi 466-8555, Japan

(Received 16 October 2013; revised 3 February 2014; accepted 17 April 2014; first published online 15 May 2014)

We experimentally investigated streamwise variations of turbulent dynamics in drag-reducing turbulent boundary layer flows following the injection of non-ionic surfactant solutions, which mainly consisted of oleyldimethylamine oxide. We focus on the comparison of turbulence statistics between injected (i.e. heterogeneous) and premixed (i.e. homogeneous) surfactant solutions, in which the maximum drag reduction ratio of 50 % is the same at the most downstream position for both cases. The wall-normal profiles of turbulence statistics, such as streamwise and wall-normal turbulence intensities, seem to be noticeably different between heterogeneous and homogeneous surfactant solutions. However, streamwise variations in these maxima and the wall-normal locations are essentially similar to one another, except for the maximum of streamwise turbulence intensity, which is not arranged by the amount of drag reduction and is also dependent on the normalization due to outer and inner variables. Such complex behaviour of streamwise turbulence intensity would be caused by the formation of near-wall layered structures that are parallel to the wall. For both heterogeneous and homogeneous surfactant solutions, the streamwise variation in the drag reduction ratio corresponds well to those of the mean velocity in wall units and the wall-normal locations of maxima of streamwise and wall-normal turbulence intensities with both outer and inner scaling. Unlike the Reynolds shear stress, the correlation coefficient of the streamwise and wall-normal turbulent fluctuations is correlated well with the drag reduction ratio. We present plausible pictures of the development of turbulence structures such as hairpin vortices and low-speed streaks for the drag-reducing turbulent boundary layer in heterogeneous and homogeneous surfactant solutions, which are comprehensively derived from the present set of experimental measurements such as flow visualization, planar laser-induced fluorescence, two-component laser-Doppler velocimetry and particle image velocimetry on the streamwise and wall-normal plane and the streamwise and spanwise plane.

Key words: drag reduction, flow control, turbulent boundary layers

1. Introduction

Surfactants are categorized into four types, namely, anionic, cationic, non-ionic and zwitterionic. Among them, cationic surfactants have been widely investigated

† Email address for correspondence: tamano.shinji@nitech.ac.jp

https://doi.org/10.1017/jfm.2014.225 Published online by Cambridge University Press

as drag-reducing additives for wall-bounded turbulent flows, since they have high drag-reducing ability of up to 80 % as reported by some reviews (see e.g. Gyr & Bewersdorff 1995; Zakin, Lu & Bewersdorff 1998). Recently, Broniarz-Press, Rozanski & Rozanska (2007) and Zakin & Ge (2010) clarified the similarities and differences of drag reduction in high-molecular-weight polymers and surfactant solutions. More recently, Li *et al.* (2012) summarized their comprehensive studies of surfactant drag reduction involving state-of-the-art experiments, numerical simulation, theoretical analysis and applications. A non-ionic surfactant is non-toxic and biodegradable, and the potential damage to the environment is much smaller than that of a cationic surfactant. As pointed out in the review by Zakin *et al.* (1998), non-ionic surfactant molecules do not carry charges and thus they are less negatively affected by other ions such as the calcium and magnesium ions normally present in tap water.

Although the drag-reducing ability of a non-ionic surfactant solution, such as heat transfer reduction (Aguilar, Gasljevic & Matthys 2001), the diameter effect (Gasljevic, Aguilar & Matthys 2001) and temporary degradation and recovery (Gasljevic, Hoyer & Matthys 2007), have been clarified, there have been few studies on velocity measurements of drag-reducing non-ionic surfactant solutions. In our recent work (Tamano *et al.* 2010), we investigated not only the drag reduction ratio, which was obtained by measuring the pressure drop and flow rate in the pipe flow of non-ionic surfactant solutions, but also the drag-reducing effect on the development of a turbulent boundary layer using two-component laser-Doppler velocimetry (LDV) and particle image velocimetry (PIV) systems. Turbulence statistics and structures for non-ionic surfactant solutions showed the behaviour of typical drag-reducing flow, such as suppression of turbulence and modification of near-wall vortices, but they were different from those of drag-reducing cationic surfactant solutions (see Tamano *et al.* 2009*b*, 2010). They showed that turbulence statistics for turbulent boundary layers of non-ionic surfactant solutions were similar to those for polymer solutions, rather than cationic solutions, in which bilayered structures of the fluctuating velocity vectors were observed in high activity. It should be noted that non-ionic and cationic surfactant aqueous solutions were homogeneous in our previous studies on the drag-reducing turbulent boundary layer flows (Itoh *et al.* 2005; Tamano *et al.* 2009*b*, 2010; Tamano & Itoh 2011).

A recent review of the drag reduction of turbulent boundary layers due to the injection of polymer was reported by White & Mungal (2008). Koskie & Tiederman (1991) investigated the drag reduction by the injection of polymer solutions for a turbulent boundary layer using LDV measurements. Fontaine, Petrie & Brungart (1992) performed the LDV and laser-induced fluorescence (LIF) measurements and found that the bursting process was suppressed by injection of polymer solutions into the near-wall region of a turbulent boundary layer. White, Somandepalli & Mungal (2004) and Hou, Somandepalli & Mungal (2008) clarified the effects of polymer additives on the turbulent boundary layer using PIV measurements. As reviewed by White & Mungal (2008), the dependence of turbulence intensity of the velocity fluctuations on the drag reduction ratio was more complex compared to the turbulent channel flow. These earlier experimental studies claimed that turbulence structures of drag-reducing turbulent boundary layer flows following polymer injection were more complex due to the history effect of the interaction between the polymer (or network structures of surfactant micelles) and the turbulence compared to those of drag-reducing turbulent channel flows, although some trends of turbulence statistics, e.g. the steeper slope of the logarithmic region of the mean velocity profile and

https://doi.org/10.1017/jfm.2014.225 Published online by Cambridge University Press

the decrease in wall-normal turbulence intensity and Reynolds shear stress with the amount of drag reduction, the modification of quasi-streamwise vortices, hairpin vortices and low-speed streaks, were similar to data obtained in internal flows.

More recently, Somandepalli, Hou & Mungal (2010) combined PIV and the planar laser-induced fluorescence (PLIF) measurements for the polymer drag-reducing turbulent boundary layer and found that the action of the polymer was to reduce the streamwise concentration fluxes, with the magnitude of the suppression increasing with concentration, and the turbulent Schmidt numbers were all greater than unity. Winkel *et al.* (2009) and Elbing *et al.* (2011, 2013) investigated the polymer drag reduction of a turbulent boundary layer at very high Reynolds numbers, which was carried out at the US Navy's William B. Morgan Large Cavitation Channel. Winkel *et al.* (2009) showed that the evolution of near-wall polymer concentration was divided into three regimes, i.e. near-injector development region, transitional region and final region. Elbing *et al.* (2011) clarified the effects of the flow-induced polymer degradation and the surface roughness, which led to a significant decrease in drag reduction. Elbing *et al.* (2013) showed that the ultimate profiles did not exhibit a logarithmic functional relationship at high-Reynolds-number as well as low-Reynolds-number flow (see also White, Dubief & Klewicki 2012).

However, the drag-reducing mechanism due to the injection of viscoelastic fluids such as polymer and surfactant solutions into turbulent boundary layer flows still remains unknown, in spite of the recent experiments mentioned above and numerical attempts based on direct numerical simulation (DNS) of drag-reducing zero-pressure-gradient turbulent boundary layer flows using the constitutive equation models (e.g. Dimitropoulos *et al.* 2005, 2006; Tamano *et al.* 2007, 2009*a*; Tamano, Graham & Morinishi 2011). For further understanding such a complex mechanism of drag reduction in turbulent boundary layers, i.e. the streamwise variations of turbulent dynamics, however, the accumulation of experimental data, especially comparison of homogeneous and heterogeneous drag reduction, is required, while such a comparison of drag reduction between homogeneous and heterogeneous polymer solutions has been reported for turbulent pipe flows (e.g. Vleggaar & Tels 1973; Frings 1988; Hoyt & Sellin 1991; Sun Chee Fore, Szwalek & Sirviente 2005). Vleggaar & Tels (1973) and Frings (1988) reported that the heterogeneous drag reduction was significantly larger than that obtained for homogeneous polymer solutions of the same average concentration. Sun Chee Fore *et al.* (2005) also reported that the polymer injection could be more or less cost-effective compared to the preparation of polymer solution, depending on the type of polymer. Dimitropoulos *et al.* (2006) investigated the drag reduction in turbulent boundary layer flow of inhomogeneous polymer solution using DNS with the FENE-P model and found that the polymer transport decreased drag reduction downstream compared to the homogeneous case. However, the Schmidt number in their study is much smaller than that (of the order of 10^5) of an actual aqueous solution of polymer because of the limitation of computational cost. So, the accumulation of experimental data is required for further understanding of the mechanism of drag reduction in turbulent boundary layers with additives.

For a polymer solution, which is very sensitive to mechanical degradation, it is very difficult to compare polymer injection data with homogeneous polymer solution data on turbulent boundary layer flow, in the case that the working fluids are circulated by a pump. Compared to the polymer solution, the non-ionic surfactant solution is much more stable, even if it shows slight degradation in a circulating water tunnel, unlike the cationic surfactant solutions (see Tamano *et al.* 2010, 2012). In this study, taking into account the fact that the non-ionic surfactant can reduce the effects on the

https://doi.org/10.1017/jfm.2014.225 Published online by Cambridge University Press

environment compared to the cationic surfactant and do not need a counterion, unlike the cationic surfactant as well as high-molecular-weight polymer, we selected the non-ionic surfactant as the drag-reducing additives. We focused on the comparison of the turbulent dynamics between homogeneous (premixed) and heterogeneous (injected) non-ionic surfactant solutions in the boundary layer, which is the first such attempt, to our knowledge. Here it should be noted that, although the concentration of surfactant solution is the same, the solution temperature is different so that the drag reduction ratio, which strongly affects the development boundary layer (see e.g. Tamano *et al.* 2009*b*), is the same at the present measurement location most downstream.

In this study, we conducted flow visualization, PLIF and two-component LDV and PIV measurements for a turbulent boundary layer with drag-reducing non-ionic surfactant injection from the wall surface. The turbulence statistics obtained by LDV measurement were normalized by both outer and inner variables. The PIV measurements were performed for both the streamwise and wall-normal (x–y) plane and the streamwise and spanwise (x–z) plane. The present paper is arranged as follows. The present experimental set-up, procedures and working fluids are described in § 2. In § 3, experimental results are presented. First, how injected surfactant solutions diffuse was investigated by the flow visualization and PLIF measurements. Next, the difference in turbulence statistics between the surfactant injection and homogeneous surfactant solution are investigated. Finally, turbulence structures for surfactant injection are discussed in relation to those of water and homogeneous surfactant solutions (see Tamano *et al.* 2010). The key results are summarized and the conclusions are given in § 4.

2. Experimental apparatus and procedure

Figure 1 shows the present experimental apparatus, which consists of the part for the circulation of working fluids and the injection part for the surfactant solution or water. The closed-loop water tunnel with a cross-section of 300 mm × 300 mm and a length of 1500 mm was used. A test plate of 20 mm × 295 mm × 1700 mm was installed in the water tunnel. All parts in contact with the surfactant solution were made of acrylic resin or stainless steel. A 2 mm diameter trip wire fixed at 100 mm downstream from the leading edge at 10° was used to develop the boundary layer on the test plate. Working fluids were circulated by a stainless steel centrifugal pump. The free-stream velocity U_e was set at approximately 300 mm s^{-1}. The angle of flap to the test plate was adjusted, so that the difference in free-stream velocities ($U_e \simeq 300$ mm s^{-1}) between the location of the leading edge of the test plate and the location 1000 mm downstream was less than 1 %. The free-stream turbulence intensity was less than 2 % owing to use of porous plates, honeycombs and mesh screens. The detailed experimental set-up except for the injection slot is referred to in our previous papers (Itoh *et al.* 2005; Tamano *et al.* 2009*b*, 2010).

Figure 2 shows the present injection slot made of stainless steel, which consists of a pressure chamber measuring 85 mm × 16 mm × 230 mm. The slit with streamwise and spanwise length of 1.0 and 200 mm was flush-mounted into the test plate. The slit, which consisted of two parallel plates with a gap of 0.5 mm, was located at $x = 300$ mm and inclined at 30° to the flat plate, which was determined by reference to Hou *et al.* (2008). The surfactant solution was injected into the turbulent boundary layer through this injection slot, which consisted of an acrylic syringe with an inner diameter of 108.5 mm, acrylic piston and vinyl chloride contracting nozzle. The piston displacement was controlled by an electric actuator (EZC4E030M-A, Oriental Motor

https://doi.org/10.1017/jfm.2014.225 Published online by Cambridge University Press

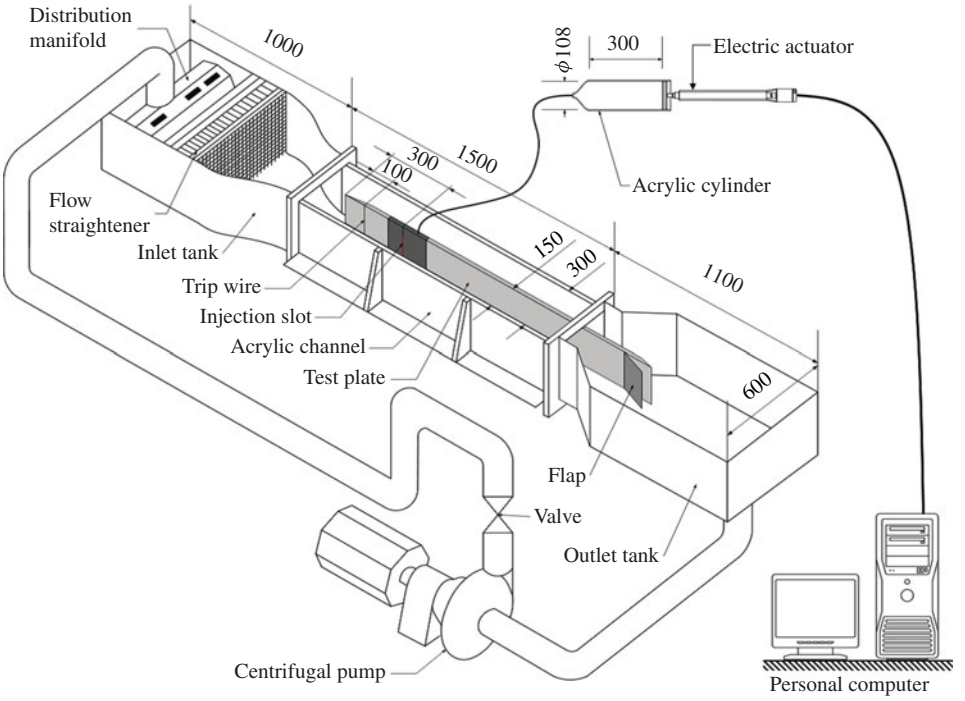


FIGURE 1. Experimental apparatus (dimensions in millimetres).

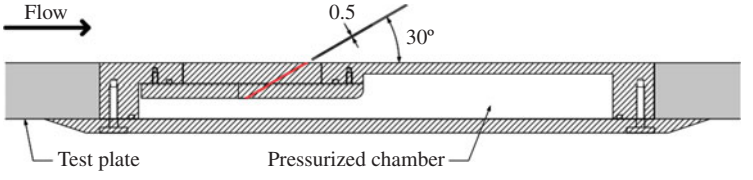


FIGURE 2. Injection slot (dimension in millimetres).

Ltd) with the PC control (ESMC-A2, Oriental Motor Ltd), in which the maximum stroke was 300 mm and the maximum speed was 300 mm s^{-1} with an accuracy of 0.01 mm s^{-1}. The flow rate of the injection Q_i was set at 1.45×10^{-2} l s^{-1}, which was comparable with the volume flow rate in the viscous sublayer and satisfies the limitation of Wu & Tulin (1972) as well as previous studies (e.g. Fontaine *et al.* 1992; Hou *et al.* 2008). We confirmed that turbulence statistics obtained by LDV measurements for turbulent boundary layer flow with the water injection were almost the same as those without the water injection (not shown in this paper).

For all measurements, such as the flow visualization, PLIF, LDV and PIV measurements, data were recorded after 17 s from the start of the injection of surfactant solution, during which time the injected surfactant solution was enough to reach the measurement streamwise locations ($x = 500$, 800 and 1000 mm) under the free-stream velocity ($U_e = 300$ mm s^{-1}). The injection of surfactant solution continued for 60 s. It should be noted that, after the end of all the measurements for the surfactant injection at different wall-normal locations, the maximum of background concentration of surfactant could be estimated to be up to approximately 70 p.p.m.

https://doi.org/10.1017/jfm.2014.225 Published online by Cambridge University Press

We confirmed that turbulence statistics without the injection after the end of the measurement for the injection of surfactant solution (i.e. homogeneous surfactant solution with the background surfactant concentration of approximately 70 p.p.m.) were almost the same as those of water without injection in water flow (i.e. the background surfactant concentration of 0 p.p.m.) using the LDV measurement (not shown here).

The flow visualization, PLIF, LDV and PIV measurements were made 500, 800 and 1000 mm downstream of the leading edge. For the case of the surfactant injection, the temperature T of the working fluids was 20 °C, and the variation of T was controlled within ± 0.3 °C during the measurements by two refrigerators (CA-2100, CA-2600, Tokyo Rikakikai Ltd).

Regarding the flow visualization, a mixture of the visualization dye (Rhodamine B, approximately 5 p.p.m.) and the working fluid was injected into the turbulent boundary layer. The streamwise and wall-normal (x–y) plane to the test plate was illuminated by a laser sheet (output 1.5 W, width 2 mm; LYPE-2SG-WL532CW, Japan Laser Ltd) through the sidewall of the channel, and images were captured by a digital video camera (EOS 7D, Canon Ltd) from the bottom of the channel. The resolution was 5184 pixels $\times$ 3456 pixels for images and 1920 pixels $\times$ 1080 pixels for movies. The frame rate was set at 30 frames per second (f.p.s.) with a shutter speed of 1/2000 s.

The PLIF measurement was performed to investigate the behaviour of diffusion of surfactant solution injected through the slit in the streamwise direction. The visualization dye (Rhodamine B) is the same as that of the flow visualization measurement. The x–y plane normal to the test plate was illuminated by a laser sheet (output 2 W, width 2 mm; DPSS Green Laser Model, DGGL-2W, Japan Laser Ltd) through the sidewall of the channel, and images were captured by a high-speed camera (FASTCAM-1024PCI, Photron Ltd) from the bottom of the channel. The resolution of the high-speed camera was set at 128 pixels $\times$ 1024 pixels in the streamwise and wall-normal directions for the region of 6.25 mm $\times$ 50 mm. The shutter speed and the frame rate were set at 1/5000 s and 1000 f.p.s., respectively. The high-speed camera and the laser sheet irradiation apparatus were fixed at the directional electrical traverse systems. In this study, the x and y directional electrical traverse systems (EXX9LH-80WA and EZX9LH-20WA, Oriental Motor Ltd) were used, in which they were orthogonally crossed and controlled by the PC controller (EZXMC-W, Oriental Motor Ltd) with an accuracy of ± 5 μm. For a single measurement, approximately 52 000 images were recorded. At the different streamwise locations ($x = 500$, 800 and 1000 mm), the PLIF measurements were repeated five times and averaged. The grey values were calculated by commercial software (Image-pro Analyzer, Nippon Roper Inc), and then the mean value and the root mean square (r.m.s.) of the fluctuation were obtained by post-processing.

The present two-component LDV system with 300 mW argon-ion laser (Model 1895, Kanomax Japan Inc.) was used in the back-scatter mode. The flow was seeded with nylon powder particles (mean diameter 4.1 μm and specific gravity 1.02). The particle concentration was approximately 5 p.p.m. for the LDV measurement. LDV measurements were made 150 mm above the channel bottom, and at locations downstream from the leading edge where $x = 500$, 800 and 1000 mm. Data samples in the locations away from and near the wall were 600 and 7200 for the injection case, respectively, which were much smaller than those of the homogeneous case (approximately 25 000 and 10 000) due to the limited duration (60 s) of the injection. In this study, the x and y traverse systems were the same as the PLIF measurements.

https://doi.org/10.1017/jfm.2014.225 Published online by Cambridge University Press

For further details of the present LDV system, readers are referred to our previous studies (see Itoh *et al.* 2005; Tamano *et al.* 2009*b*, 2010).

The two-dimensional PIV measurement on the x–y plane was made for the section normal to the test plate (the streamwise and wall-normal section), which was illuminated by a laser sheet through the sidewall of the channel, and images were captured by a high-speed camera from the bottom of the channel. The high-speed camera and the laser sheet irradiation apparatus were the same as those of PLIF measurements and fixed at the directional electrical traverse systems mentioned above. The resolution of the high-speed camera on the x–y plane was set at 1024 pixels × 1024 pixels in 50 mm × 50 mm. The frame rate was set at 1000 f.p.s. The shutter speed was 1/5000 s. The flow was seeded with particles (Orgasol, mean diameter 50 μm, specific gravity 1.03). The interrogation region was 71 pixels × 25 pixels in the streamwise and wall-normal direction, respectively. The search region was 10 pixels × 6 pixels for the x–y plane. The turbulent statistics were obtained by evaluating 52 000 images in PIV vector fields in the narrower region with 128 pixels × 1024 pixels using the PIV software (FtrPIV, Flowtech Research Inc.) and visualization software (Tecplot, Hulinks Inc.). Erroneous velocity vectors were removed, and the missing data were supplemented by interpolation of neighbouring velocity vectors. The fluctuating velocity vector fields were obtained by the Reynolds decomposition. It should be noted that the resolution of the present PIV measurement in the region close to the wall is much higher than that of our previous studies (Tamano *et al.* 2009*b*, 2010; Tamano & Itoh 2011). For the PIV measurement on the x–z plane, the laser and camera positions were interchanged in comparison with the PIV measurement on the x–y plane. The shutter speed and frame rate for the x–z plane were the same as those for the x–y plane. The resolution of the high-speed camera on the x–z plane was set at 1024 pixels × 1024 pixels in 98 mm × 98 mm. The interrogation and search regions were 51 pixels × 31 pixels and 5 pixels × 6 pixels in the streamwise and spanwise direction, respectively. For both PIV measurements on the x–y and x–z planes, the overlap ratios were varied from approximately 50 % to 80 %, which were dependent on experimental conditions and measurement locations. For further details of the present PIV systems, readers are again referred to our previous studies (Tamano *et al.* 2009*b*, 2010; Tamano & Itoh 2011).

The non-ionic surfactant, oleyldimethylamine oxide (ODMAO), forms long threadlike micelles (the network structures) in aqueous solution without any additives, unlike the cationic surfactant in which the network structures of micelles are usually formed if the counterion, e.g. sodium salicylate (NaSal), is mixed. This is the advantage of the non-ionic surfactant, in addition to its non-toxic and biodegradable properties. The non-ionic surfactant used here was Aromox (developed by Lion Akzo Co. Ltd), which consisted mainly of ODMAO, dissolved in tap water and gently stirred for four hours. The concentration of ODMAO was 500 p.p.m. by weight. The shear viscosity η of the surfactant solutions of ODMAO 500 p.p.m. was measured using a homemade capillary viscometer, in which the gravity flow was generated by the head tank of 1000 mm (see Tamano *et al.* 2012 for details). A stainless smooth pipe with an internal diameter of $d = 5.0$ mm was used. The flow rate was controlled by a needle valve and measured in terms of the weighing method. The developing region is 600 mm long ($= 120d$), and the measuring region is 1400 mm long ($= 280d$). A pressure transducer (LPM5481, GE Druck Co. Ltd) with a full scale of 200 Pa and linearity of ±0.25 % was used for measurements of pressure loss in the measuring region. The water-jacketed structure kept solution temperature variation within ±0.1 °C during shear viscosity measurements.

https://doi.org/10.1017/jfm.2014.225 Published online by Cambridge University Press

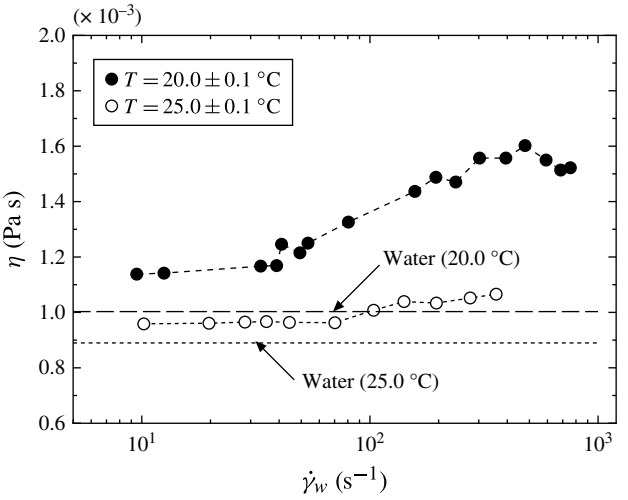


FIGURE 3. Shear viscosity versus shear rate for ODMAO 500 p.p.m.

Figure 3 shows the shear viscosity η for present non-ionic surfactant solution (ODMAO 500 p.p.m.) at $T = 20$ and 25 °C. The surfactant solution at $T = 20$ °C was used for the case of the surfactant injection, while that at $T = 25$ °C was used for the case of the homogeneous surfactant solution (see Tamano *et al.* 2010). The homogeneous surfactant solutions at $T = 20$ °C are slightly affected by mechanical degradation due to the centrifugal pump (see Tamano *et al.* 2010), while the heterogeneous surfactant solution at $T = 20$ °C is not. It should be noted again that the present experimental conditions were determined to make it possible to compare the development of turbulence dynamics between homogeneous and heterogeneous systems under the condition that the drag reduction ratio downstream (at $x = 1000$ mm) was the same (see figure 8 for details). For the case of surfactant injection, the shear viscosity η at $T = 25$ °C increases with increase in the shear rate from $\dot{\gamma}_w = 40$ s^{-1}, while the shear viscosity η at $T = 20$ °C slightly increases with increase in the shear rate $\dot{\gamma}_w > 70$ s^{-1}. It is well known that the sudden increase in η around a critical shear rate is a typical indication of shear-induced structure (SIS), which is closely related to the viscoelasticity and the drag-reducing ability for the typical drag-reducing cationic surfactant additives (see e.g. Qi & Zakin 2002). On the other hand, the rheological property of a drag-reducing non-ionic surfactant solution and its SIS formation have not been well investigated (Hu & Matthys 1997). In particular, the relation between the elongational viscosity of drag-reducing non-ionic surfactant and the turbulent drag reduction remains unknown. This may be due to the difficulty of the measurement of the elongational viscosity of dilute solutions. It has been reported, however, that the larger elongational viscosity was responsible for the higher drag reduction ratio for polymer solutions (e.g. Escudier, Presti & Smith 1999; Bonn *et al.* 2005; Wagner *et al.* 2006) and cationic surfactant solutions (e.g. Lu *et al.* 1998*a*,*b*; Lin *et al.* 2000; Qi & Zakin 2002; Drappier *et al.* 2006). Moreover, recent DNS studies on wall-bounded turbulent flows have supported the suggestion that the elongational viscosity was the key parameter for drag reduction (e.g. Dimitropoulos, Sureshkumar & Beris 1998; Housiadas & Beris 2004; Li, Sureshkumar & Khomami 2006*a*; Tamano *et al.* 2009*a*). The effects of concentration, temperature and degradation on the drag reduction ratio of the non-ionic surfactant solutions used here can be found in Tamano *et al.* (2012).

https://doi.org/10.1017/jfm.2014.225 Published online by Cambridge University Press

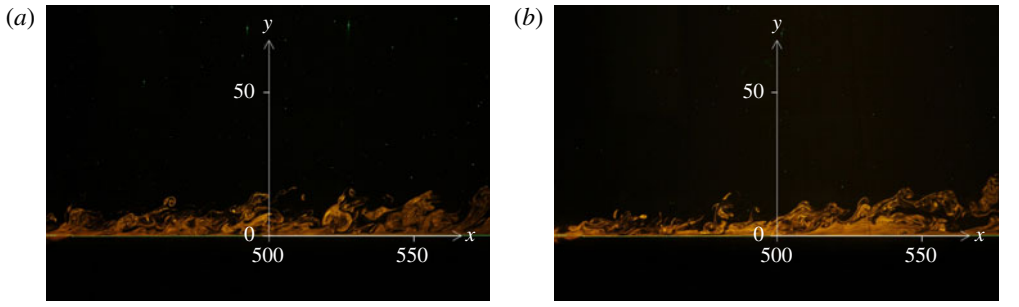


FIGURE 4. Flow visualization measurements on the x–y plane around $x = 500$ mm: (a) water injection; (b) surfactant injection ($C = 500$ p.p.m.); unit (mm).

Evaluation of the friction velocity at the different streamwise locations in turbulent boundary layer flows (see § 3 for details) requires a value of the kinetic viscosity that depends on the shear rate and varies in the streamwise direction for the turbulent boundary layer. Since the mean velocity gradient at the wall $\mathrm{d}U/\mathrm{d}y|_{wall}$ is not constant, unlike for the fully developed turbulent channel flow, we obtained the kinetic viscosity at the wall as follows. First, the value of $\mathrm{d}U/\mathrm{d}y|_{wall}$ was estimated by the mean velocity near the wall, which was obtained by the LDV measurement. Second, the shear viscosity η at the wall was determined by using the shear viscosity measurements obtained by a capillary viscometer. Finally, the kinetic viscosity $\nu = \mu/\rho$ at the wall was obtained, in which the density ρ of water at the same temperature was used. Here, it should be noted that, even for the surfactant injection case, the concentration of surfactant additives at the wall was supposed to be constant at the different streamwise locations ($x = 500$, 800 and 1000 mm), because we could not know the precise local concentration at the wall owing to the limited accuracy of the PLIF measurements. For the case of surfactant injection, the concentration at the wall could be roughly estimated to be between 400 and 500 p.p.m. from preliminary experiments (see also the last paragraph of § 3.1 for details), and then we considered that the effect of the variation of the kinetic viscosity would be negligible. Recently, Cai, Suzuki & Komoda (2012) reported that there was a critical concentration of the ODMAO solution, around 400 p.p.m., below which structure formation and shear thickening behaviour did not appear. It is noted that the local concentration at the wall in the present boundary layer flow may be just above this critical concentration. Tamano *et al.* (2012) also showed the effects of solution concentration from 50 to 1000 p.p.m., solution temperature from 10 to 40 °C, and degradation on drag reduction of ODMAO solutions, and then examined the relation between drag-reducing effects and the strength of the shear thickening. For the exact estimation of the local kinetic viscosity, however, we must measure the shear viscosity of surfactant solutions with a considerably different range of concentration below 500 p.p.m., which is beyond the limits of the present study.

3. Results

3.1. *Flow visualization and PLIF measurements with surfactant injection*

Figures 4 and 5 show the flow visualization results on the x–y plane around $x = 500$ and 1000 mm, respectively, for water and non-ionic surfactant (ODMAO) injections. Flow is from left to right. In the figures, $y = 0$ is the location of the wall. For

https://doi.org/10.1017/jfm.2014.225 Published online by Cambridge University Press

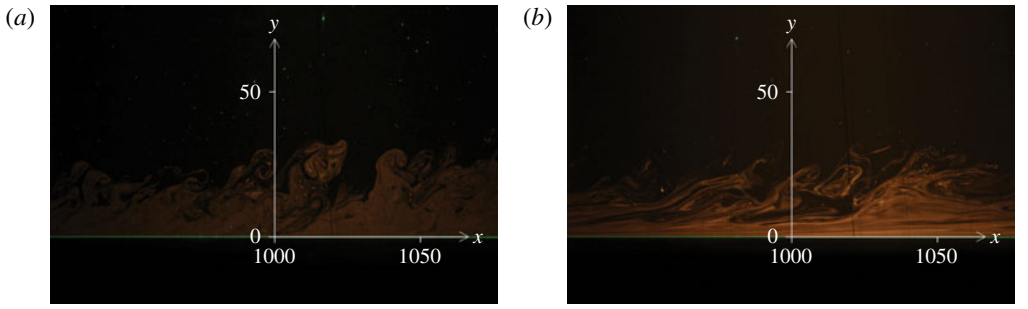


FIGURE 5. Flow visualization measurements on the x–y plane around $x = 1000$ mm: (a) water injection; (b) surfactant injection ($C = 500$ p.p.m.); unit (mm).

the water injection at both $x = 500$ and 1000 mm, flow visualization dye displays a very complex behaviour, which indicates that the potential and turbulent flows are strongly mixed, in which the emission of the visualization dye at $x = 1000$ mm is weaker than that at $x = 500$ mm due to the diffusion effect. For the surfactant injection, the behaviour of the flow visualization dye is quite similar to that of water at $x = 500$ mm. At $x = 1000$ mm, on the other hand, the flow visualization dye near the wall seems to be almost parallel to the wall, unlike the corresponding situation for water, which indicates that the layered structure is formed and also suggests that the wall-normal momentum transfer is strongly attenuated due to surfactant injection. The layered structure is a typical feature of drag-reducing flows with the large drag reduction ratio DR (the definition is explained later), as pointed out in our previous studies (Tamano *et al.* 2009*b*, 2010; Tamano & Itoh 2011). The present layered structure is also similar to the sheet-like structure presented by Samanta *et al.* (2013), who investigated the elasto-inertial turbulence in which polymers were extended in sheet-like regions of large streamwise and spanwise dimensions and such sheets produced greater polymer extension. Quite recently, Dubief, Terrapon & Soria (2013) also proposed the mechanism of elasto-inertial turbulence, which consisted of alternating spanwise cylindrical regions of rotational and extensional regions.

Figure 6(a) shows approximate curves of the mean grey value $\overline{I}/I_{max}$ obtained by the PLIF measurements. In the figure, δ is the boundary layer thickness. The I_{max} represents the maximum of grey value of 255 in this study. For both water and surfactant injection at all streamwise locations, the $\overline{I}/I_{max}$ value decreases monotonically away from the wall and maxima are observed at the wall. The values of $\overline{I}/I_{max}$ for water injection are smaller than those for surfactant injection at the corresponding locations, which means that the diffusion of the injected surfactant solution is suppressed more than the water injection. For the water injection, the profiles of $\overline{I}/I_{max}$ at $x = 800$ and 1000 mm are similar to each other and vary only slightly in the wall-normal direction. This indicates that the injected water is well mixed and is almost homogeneous across the boundary layer around $x = 800$ mm. For the surfactant injection, on the other hand, the wall-normal gradient of $\overline{I}/I_{max}$ across the boundary layer becomes smaller downstream, which suggests that the injected surfactant solution is still in the diffusion process even at $x = 1000$ mm.

Figure 6(b) shows approximate curves of r.m.s. of grey value fluctuation I'_{rms}/I_{max}. Regardless of the streamwise location, the value of I'_{rms}/I_{max} for surfactant injection is larger than that for water injection, which is consistent with the result that the gradient of $\overline{I}/I_{max}$ for surfactant injection is steeper than that for water injection (cf. figure 6a).

https://doi.org/10.1017/jfm.2014.225 Published online by Cambridge University Press

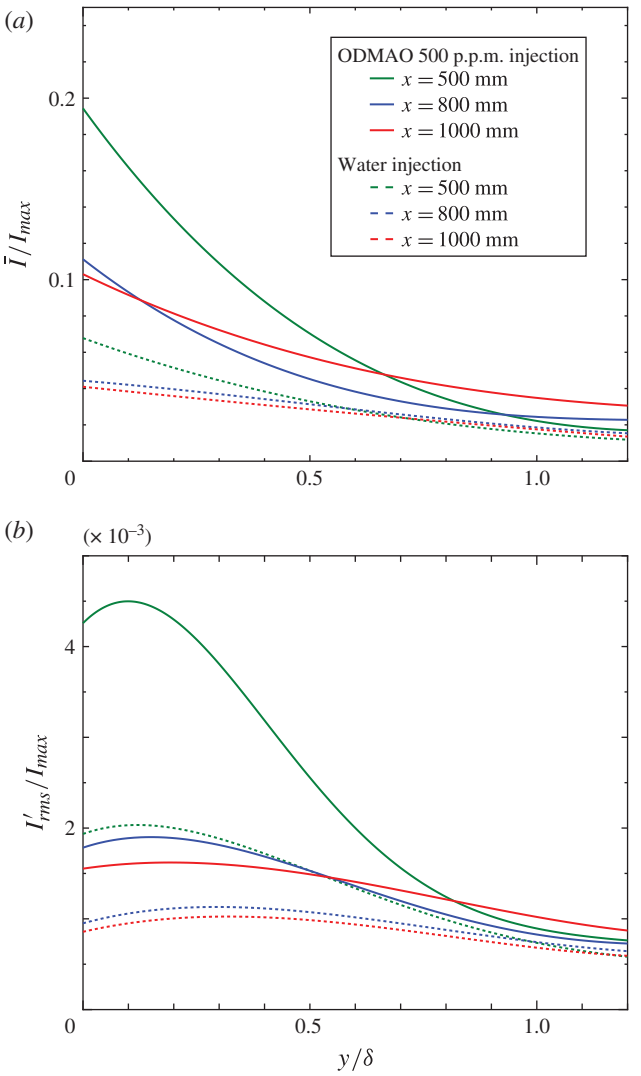


FIGURE 6. (Colour online) Grey value profiles obtained by PLIF measurements: (*a*) mean grey value; (*b*) r.m.s. of grey value fluctuation. Solid and dotted lines are approximate curves for surfactant and water injections, respectively.

For surfactant injection, a distinct maximum of I'_{rms}/I_{max} appears near the wall at $x =$ 500 mm, and it becomes ambiguous downstream.

The present profiles of $\bar{I}/I_{max}$ and I'_{rms}/I_{max} for the injected non-ionic surfactant solution are consistent with those of the injected polymer concentration profiles of Somandepalli *et al.* (2010). They reported that the action of the injected polymer was to reduce the diffusivity of the liquid close to the wall, and then the injected liquid remained confined to the inner near-wall region of the boundary layer. Here, one should note the relation between the mean grey value $\bar{I}/I_{max}$ and the mean concentration of surfactant solution, $C = 500(\bar{I}/I_{max})^{6.76\times10^{-2}}$ p.p.m., which is derived by the preliminary experiments for the injection of surfactant with concentration of 10, 50, 100, 200, 300, 400 and 500 p.p.m. under the same experimental conditions.

https://doi.org/10.1017/jfm.2014.225 Published online by Cambridge University Press

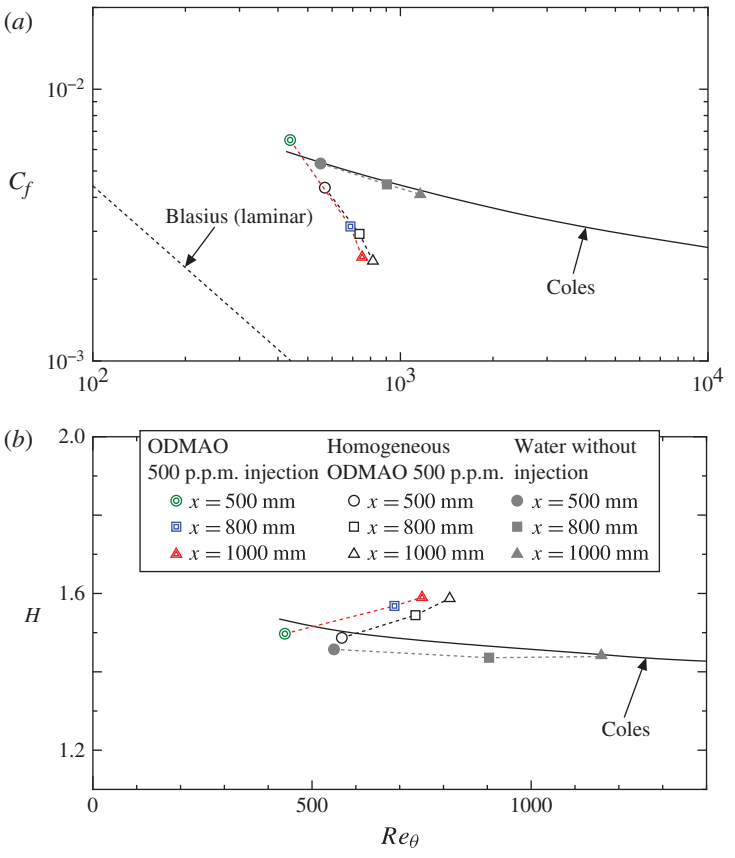


FIGURE 7. (Colour online) Boundary layer development: (*a*) shape factor versus momentum-thickness Reynolds number; (*b*) friction coefficient versus momentum-thickness Reynolds number.

The values of $\bar{I}/I_{max} = 0.1$ and 0.2 correspond to approximately $C = 430$ and 450 p.p.m., respectively. So, it can be deduced that the local solution concentration at $x = 1000$ mm for the turbulent boundary layer flow with surfactant injection is slightly lower than for the homogeneous surfactant case ($C = 500$ p.p.m.).

3.2. *Comparison of development of turbulence statistics between homogeneous and heterogeneous non-ionic surfactant solutions*

Figure 7 shows the dependence of the friction coefficient $C_f = 2(u_\tau/U_e)^2$ and shape factor $H = \delta^*/\theta$ on the momentum-thickness Reynolds number $Re_\theta = U_e\theta/\nu$, where $u_\tau = \sqrt{\tau_w/\rho}$ is the friction velocity, θ is the momentum thickness and δ^* is the displacement thickness. The wall shear stress τ_w was determined by the mean velocity gradient, which was obtained by the least-squares approximation using mean velocity measurements (three to eight points) at different wall-normal locations from the wall within the viscous sublayer ($y^+ < 5$), where $y^+ = u_\tau y/\nu$ is the distance from the wall scaled by the viscous length scale. In the case of drag-reducing surfactant solutions, the dimensional length of the viscous sublayer becomes larger with increase in *DR*. Therefore, we can obtain the mean velocity gradient near the wall for surfactant

https://doi.org/10.1017/jfm.2014.225 Published online by Cambridge University Press

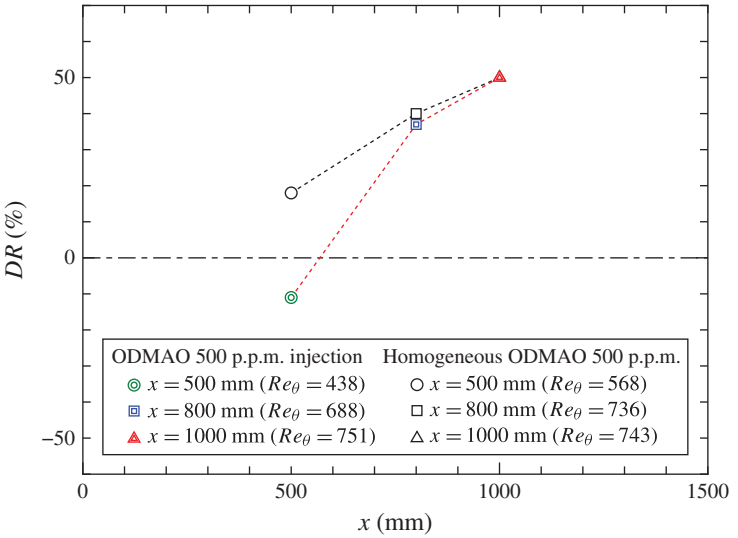


FIGURE 8. (Colour online) Streamwise variation in drag reduction ratio.

solutions more accurately, compared to water. The kinematic viscosity $\nu = \mu/\rho$ at the wall is also determined using the shear viscosity μ at the wall shear rate, which is estimated from the extrapolation of the mean velocity by LDV measurement for turbulent boundary layer flows. In figure 7, the solid and dashed lines represent Coles' curve (Coles 1962) and the Blasius laminar line, respectively. The data of C_f and H for water without injection (just water below) agree well with Coles' curves. The data of C_f versus the Reynolds number Re_θ are almost collapsed for both surfactant injection and homogeneous surfactant solutions, in which C_f drastically decreases with increasing Re_θ. In addition, H tends to increase with increase in Re_θ for both cases, although the value of H for surfactant injection is slightly higher than that for homogeneous surfactant. These results show that the development of the turbulent boundary layer parameters such as C_f and H is essentially the same for homogeneous and heterogeneous non-ionic surfactant solutions in the present study, in which the maximum drag reduction is the same, as described below.

In the present study, the drag reduction ratio DR for the turbulent boundary layer is defined as

$$DR = \frac{C_{f,water} - C_{f,surfactant}}{C_{f,water}} \times 100, \tag{3.1}$$

under the condition of the same momentum-thickness Reynolds number Re_θ. The C_f for water is obtained using the Coles' curve at the corresponding Reynolds number. Figure 8 shows the streamwise variation in the drag reduction ratio DR, in which the error bar of DR is estimated to be $\pm 5\,\%$. The streamwise variation in DR from $x = 500$ to 800 mm for the injection case is steeper than that for the homogeneous case, and it is almost the same for both cases from $x = 800$ to 1000 mm. The difference in the variation of DR from $x = 500$ to 800 mm would be mainly due to the effect of the difference in the Reynolds number, since the streamwise variation in C_f versus Re_θ is almost the same for the surfactant injection and homogeneous surfactant cases (see figure 7*a*), in which the value of DR at $x = 1000$ mm is the same and the maximum ($DR = 50\,\%$). This means that the surfactant injection method is more effective to

https://doi.org/10.1017/jfm.2014.225 Published online by Cambridge University Press

obtain the drag reduction effect than the homogeneous surfactant method, taking into account the amount of surfactant additives used. For a closer comparison, however, we should take into account the energy loss due to the movement of the piston by the electric actuator for the surfactant injection.

It should also be noted that the drag reduction ratio DR at $x = 500$ mm is negative. The negative DR is not due to the disturbance unfavourably induced by the injection of fluid into the boundary layer as mentioned in § 2. Rather, it is because the drag-increasing effect caused by the increase in the apparent kinematic viscosity due to the injection of surfactant solution overcomes the drag-reducing effect, which leads to the suppression of near-wall turbulence structures in the high drag reduction case (see § 4 for further discussion). The main difference between the heterogeneous and homogeneous cases at $x = 500$ mm is in the upstream turbulence structures of the flow approaching the area of interest. For the heterogeneous case, the increase in the apparent kinematic viscosity might be caused by the modification of turbulent structures that change from those of a Newtonian flow into those of a drag-reduced flow, giving rise to a drag-increasing effect. This scenario is supported by the recent DNS studies (see Dimitropoulos *et al.* 2005, 2006; Tamano *et al.* 2007, 2009*a*, 2011), in which the friction drag increases in the inlet region due to the sudden change of velocity fields caused by the artificial inlet boundary condition in which the velocity field data of a Newtonian fluid in the driver part are used directly. For the homogeneous case, on the other hand, there is no such significant change of turbulence structures. The present result of non-ionic surfactant injection into the turbulent boundary layer flow of water is also consistent with the study of polymer injection into the turbulent channel flow of water by Tiederman, Luchik & Bogard (1985), who showed that there was a significant drag increase in the immediate vicinity of the slot. They reported that there were two factors yielding the drag increase. One is that the viscosity of polymer solution is higher than that of water. The second is that an unmixed fluid layer along the wall will accelerate the mainstream water flow. It is noted that the latter is only applicable to the inner flow. In the present study, there is a further possibility that up to $x = 500$ mm the surfactant has not significantly penetrated the buffer region in the boundary layer with a significant concentration to cause the structures responsible for added resistance to the eddies thereby leading to drag reduction. As a result, up to that point, it appears that the main effect of the surfactant is the shear thickening one, leading to the drag increase. More detailed investigations of the relationship between the rheological properties of dilute surfactant solutions and turbulence structures are needed to further discuss the drag increase near the injection slot.

Figure 9(*a*) shows the profile of mean velocity scaled by the friction velocity $U^+ = U/u_\tau$. The dashed line shows the Newtonian log law, and the dotted line represents the Virk log law, which is Virk's (1975) ultimate profile ($U^+ = 11.7 \ln y^+ - 17$) for polymer solutions. It is seen that, on going downstream or with the increase in the amount of drag reduction, the mean velocity U^+ increases and the slope at $y^+ > 10$ becomes larger for both heterogeneous and homogeneous surfactant solutions. Much of the previous experimental data (e.g. Warholic, Schmidt & Hanratty 1999; Itoh *et al.* 2005; Tamano *et al.* 2009*b*, 2010) and DNS data (e.g. Dimitropoulos *et al.* 2005, 2006; Tamano *et al.* 2007, 2009*a*, 2011) underscore the fact that the U^+ value increases with increasing drag reduction ratio DR, which is independent of the homogeneous or heterogeneous surfactant solution. In the downstream region at $x = 800$ and 1000 mm, the mean velocities for surfactant injection agree well with those of homogeneous surfactant solutions at the corresponding streamwise locations.

https://doi.org/10.1017/jfm.2014.225 Published online by Cambridge University Press

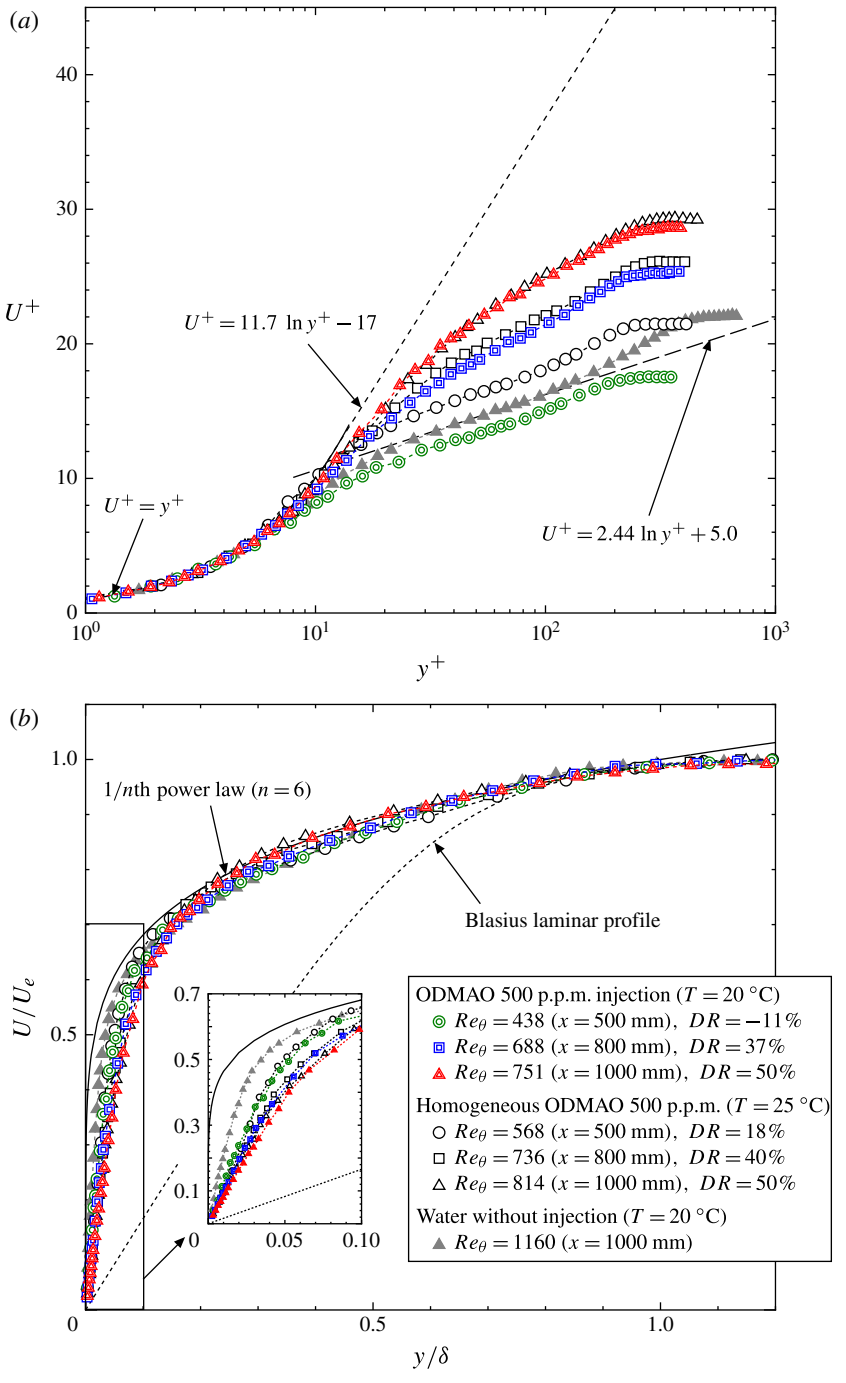


FIGURE 9. (Colour online) Mean velocity profiles: (*a*) inner scaling; (*b*) outer scaling.

The distributions of mean velocities scaled by the free-stream velocity U/U_e are shown in figure 9(*b*). The abscissa y/δ is the distance from the wall scaled by the boundary layer thickness δ. In figure 9(*b*), the solid and dotted lines represent $1/n$th power law ($n = 6$) and the Blasius laminar profile, respectively. For homogeneous and

https://doi.org/10.1017/jfm.2014.225 Published online by Cambridge University Press

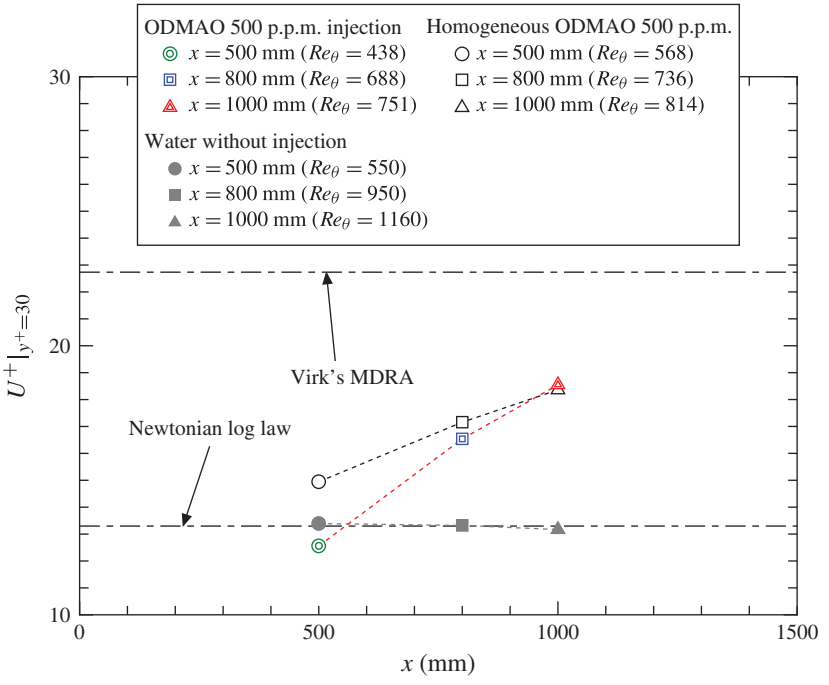


FIGURE 10. (Colour online) Streamwise variation in mean velocity with inner scaling U^+ at $y^+ = 30$.

heterogeneous surfactant solutions, the profiles of the mean velocity with outer scaling seem to be similar to each other, in that they are somewhat smaller than that for water near the wall ($y/\delta < 0.2$) and slightly closer to the Blasius laminar profile with increase in DR.

Next, we investigate streamwise variations in mean velocity profiles at $y^+ = 30$, around which the near-wall turbulent activity is large for the drag-reducing flow of viscoelastic fluids (see Tamano *et al.* 2011). In figure 10, the solid and dashed lines represent the Virk and Newtonian log laws, respectively. For the Newtonian fluid, mean velocities scaled by the friction velocity at $y^+ = 30$, values of $U^+|_{y^+=30}$ are almost constant and agree well with the Newtonian log law. For both homogeneous and heterogeneous surfactant solutions, $U^+|_{y^+=30}$ gradually increases in the streamwise direction and approaches the Virk log-law value, although the difference from the Virk log law is still large even at $x = 1000$ mm. The important finding is that streamwise profiles of $U^+|_{y^+=30}$ are similar to those of drag reduction ratio DR (cf. figure 8) as pointed out by the DNS of Tamano *et al.* (2011).

Figure 11(*a*,*b*) shows distributions of streamwise turbulence intensity scaled by the friction velocity and free-stream velocity, $u'^+_{rms} = u'_{rms}/u_\tau$ and u'_{rms}/U_e, respectively. The profiles of streamwise turbulence intensity with both inner and outer scaling seem to be different between homogeneous and heterogeneous surfactant solutions.

For easy trouble-free comparison of streamwise turbulence intensities between homogeneous and heterogeneous surfactant solutions, we focus on the streamwise variations in maxima of streamwise turbulence intensities with inner and outer scaling, $u'^+_{rms}|_{max}$ and $u'_{rms}/U_e|_{max}$ (see figure 12). Regarding the homogeneous surfactant solutions, the maximum of the streamwise turbulence intensity increases in the streamwise direction for the case of the inner scaling but is almost constant for the

https://doi.org/10.1017/jfm.2014.225 Published online by Cambridge University Press

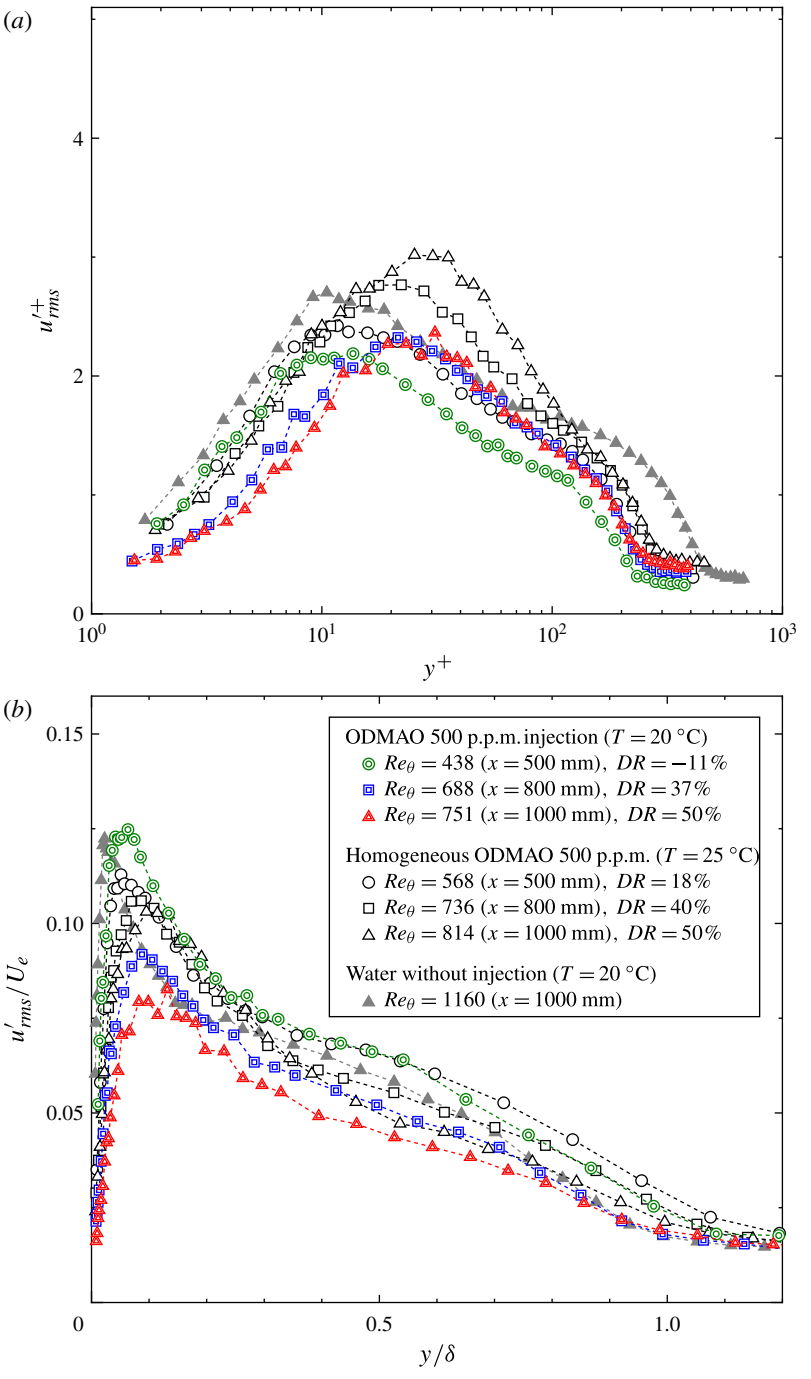


FIGURE 11. (Colour online) Streamwise turbulence intensity profiles: (*a*) inner scaling; (*b*) outer scaling.

case of the outer scaling. Regarding the surfactant injection, on the other hand, the maximum is almost constant for the inner scaling, like water, but decreases for the outer scaling. It should be noted that the streamwise variation of the maximum of

https://doi.org/10.1017/jfm.2014.225 Published online by Cambridge University Press

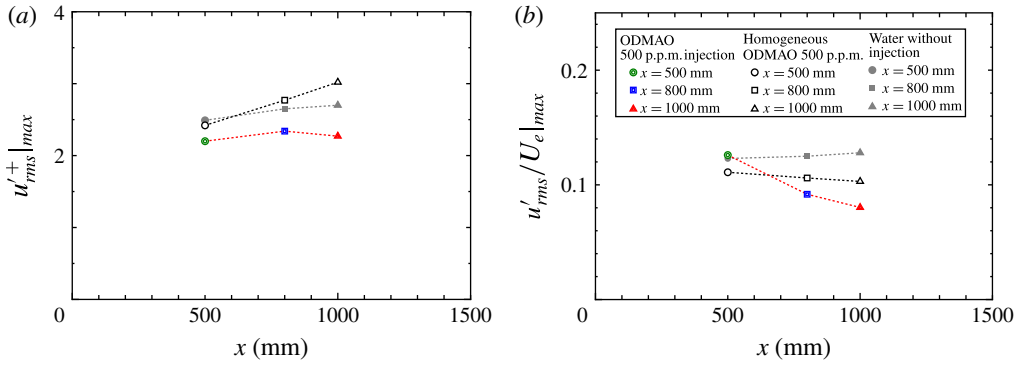


FIGURE 12. (Colour online) Streamwise variation in maxima of streamwise turbulence intensities: (*a*) inner scaling; (*b*) outer scaling.

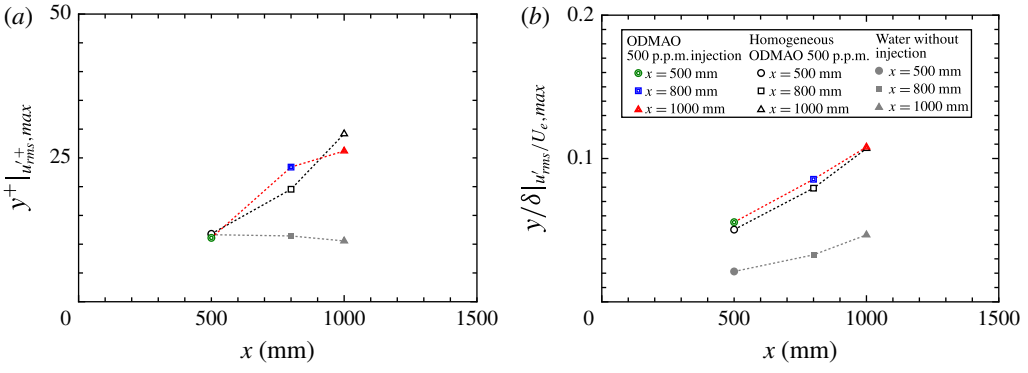


FIGURE 13. (Colour online) Streamwise variation in wall-normal locations at maxima of streamwise turbulence intensities: (*a*) inner scaling; (*b*) outer scaling.

streamwise turbulence intensity does not correspond to that of DR, e.g. the maximum of u'^{+}_{rms} for the surfactant injection at $x = 1000$ mm is smaller than that of the corresponding water, while for the homogeneous surfactant solution it is larger, even if the drag reduction ratio is the same ($DR = 50\,\%$) there. These results clearly indicate that the behaviour of streamwise turbulence intensity is strongly dependent on both how the boundary layer develops and how to normalize it, which is consistent with previous studies (e.g. Hou *et al.* 2008; White & Mungal 2008; Tamano *et al.* 2009*b*) in which the streamwise turbulence intensity is very sensitive to Re_θ, DR and how the turbulent boundary layer develops. The difference in the streamwise variation between homogeneous and heterogeneous surfactant solutions would be affected not only by the degree of diffusion of injected surfactant solution but also by the difference in rheological properties due to the difference in solution temperature and the degree of degradation of the non-ionic surfactant solution used here.

Figure 13(*a*,*b*) shows the streamwise variations in wall-normal locations at the maxima with inner and outer scaling, $y^+|_{u'^{+}_{rms},max}$ and $y/\delta|_{u'_{rms}/U_e,max}$, respectively. The locations of maxima of u'^{+}_{rms} and u'_{rms}/U_e increase monotonically on going downstream for both the surfactant injection and homogeneous surfactant solution, and these locations downstream are far away from the wall compared to the

https://doi.org/10.1017/jfm.2014.225 Published online by Cambridge University Press

corresponding situation for water. This behaviour corresponds well to that of the drag reduction ratio, and is consistent with previous experimental and numerical studies, in which the maximum of streamwise turbulence intensity moves away from the wall with increasing drag reduction ratio (e.g. Tamano *et al.* 2009*b*). Interestingly, the streamwise variation in the wall-normal location of the maximum of streamwise turbulence intensity is almost independent of both the normalization and the additive method of surfactant, which strongly influence the streamwise variation of the maximum (cf. figure 12).

Figure 14 shows the distributions of wall-normal turbulence intensities with inner and outer scaling, v'^{+}_{rms} and v'_{rms}/U_e. For both the surfactant injection and homogeneous surfactant cases, v'^{+}_{rms} gradually decreases in the streamwise direction, although v'^{+}_{rms} for the homogeneous surfactant solution seems to saturate at $x = 800$ mm. Unlike the behaviour of the maximum streamwise turbulence intensity, the maxima of wall-normal turbulence intensity for both cases decrease and the wall-normal locations of the maximum increase in the streamwise direction.

Figures 15 and 16 show the streamwise variations in maxima of wall-normal turbulence intensities with inner and outer scaling, $v'^{+}_{rms}|_{max}$ and $v'_{rms}/U_e|_{max}$ and the streamwise variations in wall-normal locations at the maxima, $y^{+}|_{v'^{+}_{rms},max}$ and $y/\delta|_{v'_{rms}/U_e,max}$, respectively. For both surfactant injection and homogeneous surfactant cases, $v'^{+}_{rms}|_{max}$ and $v'_{rms}/U_e|_{max}$ roughly decrease in the streamwise direction, and $y^{+}|_{v'^{+}_{rms},max}$ and $y/\delta|_{v'_{rms}/U_e,max}$ monotonically move away from the wall. It is noted that the behaviour of the development is almost the same for surfactant injection and homogeneous surfactant cases, although the wall-normal profiles of wall-normal turbulence intensities seem to be different at the same streamwise location (figure 14). It is also found that the variations in both $y^{+}|_{v'^{+}_{rms},max}$ and $y/\delta|_{v'_{rms}/U_e,max}$ from $x = 800$ to 1000 mm are smaller than those from $x = 500$ to 800 mm. This behaviour is consistent with that of the drag reduction ratio DR (cf. figure 8), in which the variation in DR from $x = 800$ to 1000 mm is smaller than that from $x = 500$ to 800 mm.

Figure 17 shows the distributions of Reynolds shear stress with inner and outer scaling, $-\overline{u'v'}^{+} = -\overline{u'v'}/u_\tau^2$ and $-\overline{u'v'}/U_e^2$. Even though the data on the Reynolds shear stress seem to be scattered compared with the other turbulence statistics, as a whole, the maximum of the Reynolds shear stress, regardless of scaling, decreases with the increase in the streamwise position x (i.e. DR) and moves away from the wall, except for the homogeneous case at $x = 800$ and 1000 mm, in which the profile of the Reynolds shear stress at $x = 1000$ mm is similar to that at $x = 800$ mm, i.e. the profile seems to be saturated. At $x = 500$ mm, the Reynolds shear stress with outer scaling for the surfactant injection case ($DR = -11\,\%$) is almost comparable with that for water and is larger than that for homogeneous surfactant solution. On the other hand, the Reynolds shear stress with inner scaling for surfactant injection at $x = 500$ mm is smaller than that for water and is comparable to that for homogeneous surfactant solution. This is because the local kinetic viscosity ν becomes larger than that for water owing to the increase in the shear viscosity caused by the injection of surfactant solution (see § 2) so that the friction velocity u_τ for surfactant injection is larger than that for water at $x = 500$ mm, which causes the negative DR. At $x = 1000$ mm, the Reynolds shear stresses with inner and outer scaling for both homogeneous and heterogeneous surfactant solutions are much smaller than those of the corresponding situation for water. For the case of surfactant injection at $x = 1000$ mm ($DR = 50\,\%$), the plateau region of $-\overline{u'v'}^{+}$ is observed in the buffer region ($30 < y^{+} < 70$), while such behaviour cannot be observed for the homogeneous

https://doi.org/10.1017/jfm.2014.225 Published online by Cambridge University Press

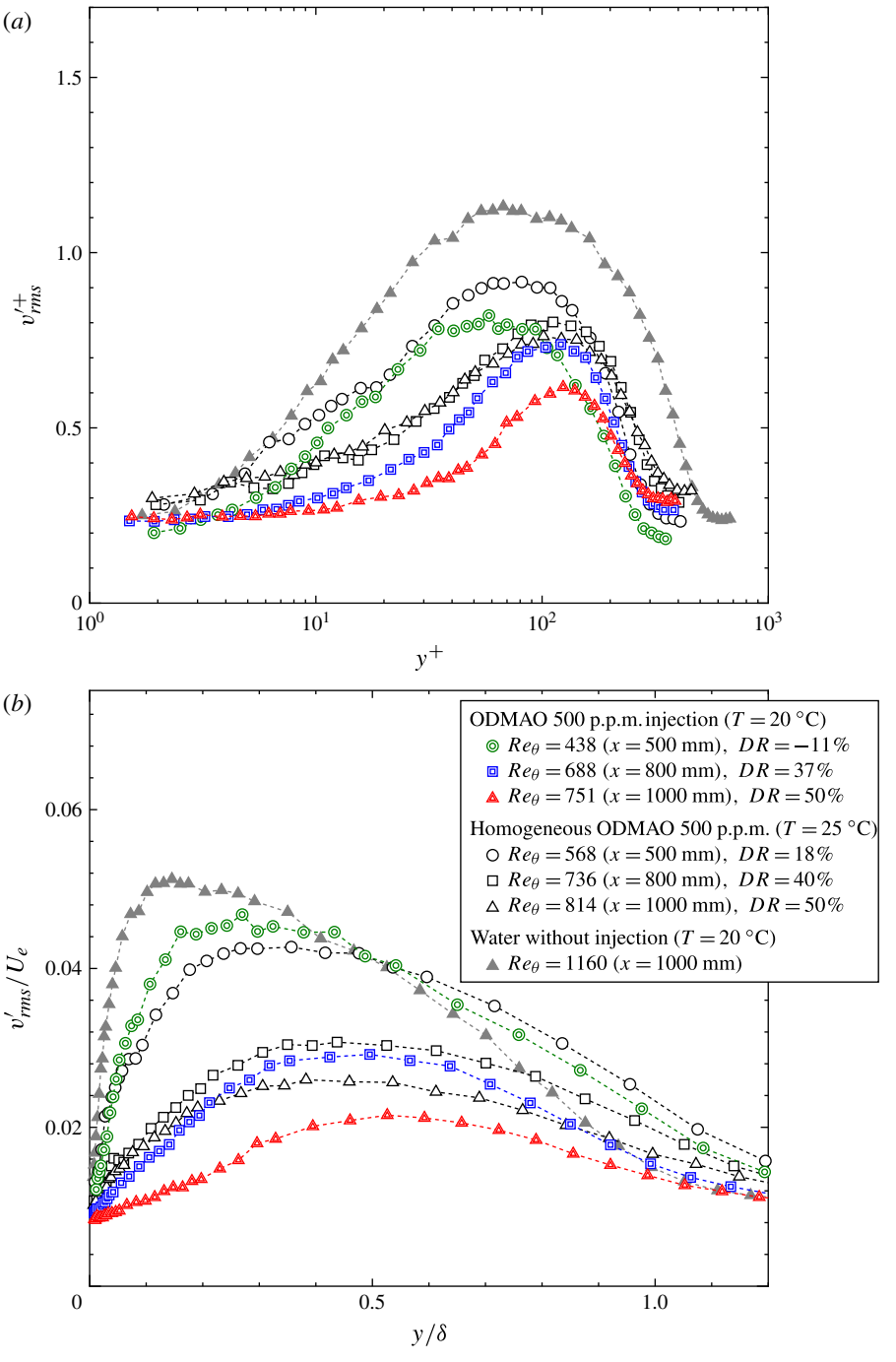


FIGURE 14. (Colour online) Wall-normal turbulence intensity profiles: (*a*) inner scaling; (*b*) outer scaling.

surfactant solution. Even though the drag reduction ratio is the same ($DR = 50\,\%$) at $x = 1000$ mm, the Reynolds shear stress of the surfactant injection is smaller than that of the homogeneous surfactant solution, which is independent of the scaling.

https://doi.org/10.1017/jfm.2014.225 Published online by Cambridge University Press

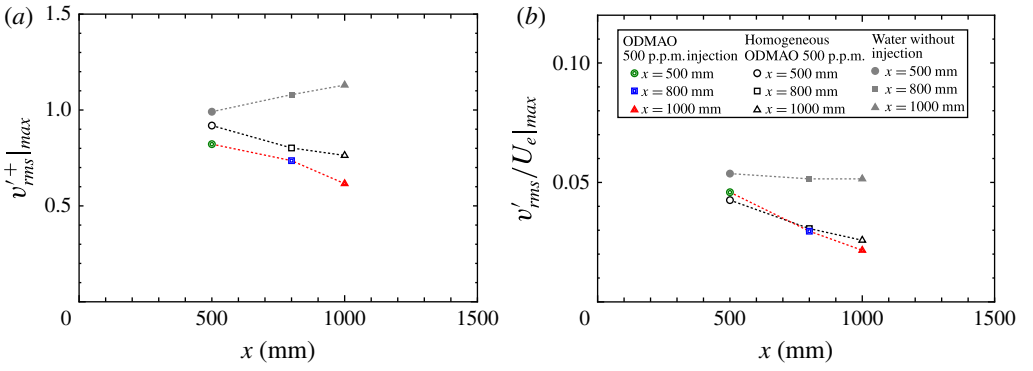


FIGURE 15. (Colour online) Streamwise variation in maxima of wall-normal turbulence intensity: (*a*) inner scaling; (*b*) outer scaling.

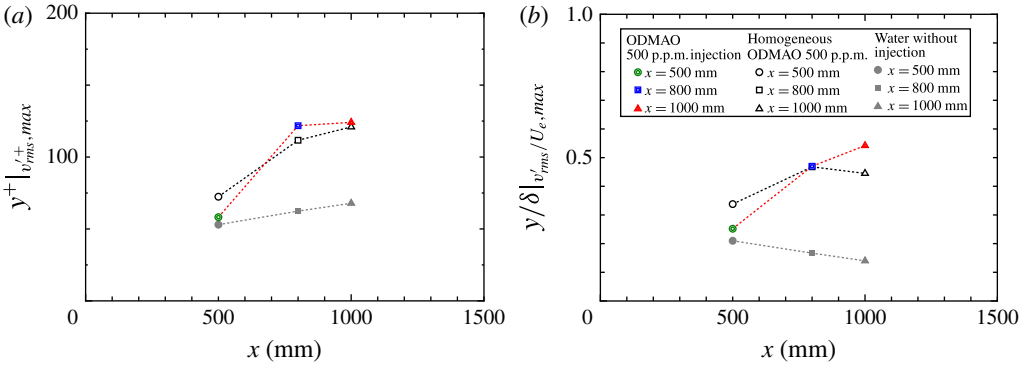


FIGURE 16. (Colour online) Streamwise variation in wall-normal locations at maxima of wall-normal turbulence intensity: (*a*) inner scaling; (*b*) outer scaling.

This indicates that the Reynolds shear stress profile for the turbulent boundary layer cannot be explained by only the amount of drag reduction.

Figure 18 shows the distributions of the correlation coefficient of the streamwise and wall-normal turbulent fluctuations, $R_{u'v'} = -\overline{u'v'}/(u'_{rms}v'_{rms})$. Except for the surfactant injection case at $x = 500$ mm, where the drag reduction ratio is negative, the $R_{u'v'}$ values for all cases with positive DR are smaller than those for the corresponding water at $y/\delta < 0.5$. It is noted that the profiles of $R_{u'v'}$ at $x = 800$ and 1000 mm for the surfactant injection case are almost the same as those for the homogeneous case, unlike the Reynolds shear stress profiles (cf. figure 17), which are dependent on the scaling. It can be concluded that the drag reduction ratio DR is closely correlated not with the Reynolds shear stress scaled by inner and outer variables but with the correlation coefficient $R_{u'v'}$, which would be a more universal profile and a better indicator of the degree of drag reduction.

The total shear stress is the sum of viscous shear stress $\mathrm{d}U^+/\mathrm{d}y^+$, turbulent shear $-\overline{u'v'}^+$ and viscoelastic stress due to polymer or surfactant micelle τ_v (see e.g. Warholic *et al.* 1999). It is almost impossible to measure the viscoelastic stress τ_v directly and accurately for real turbulent boundary flow. Therefore, if the total shear stress can be obtained, the viscoelastic stress can be obtained (Hou, Somandepalli &

https://doi.org/10.1017/jfm.2014.225 Published online by Cambridge University Press

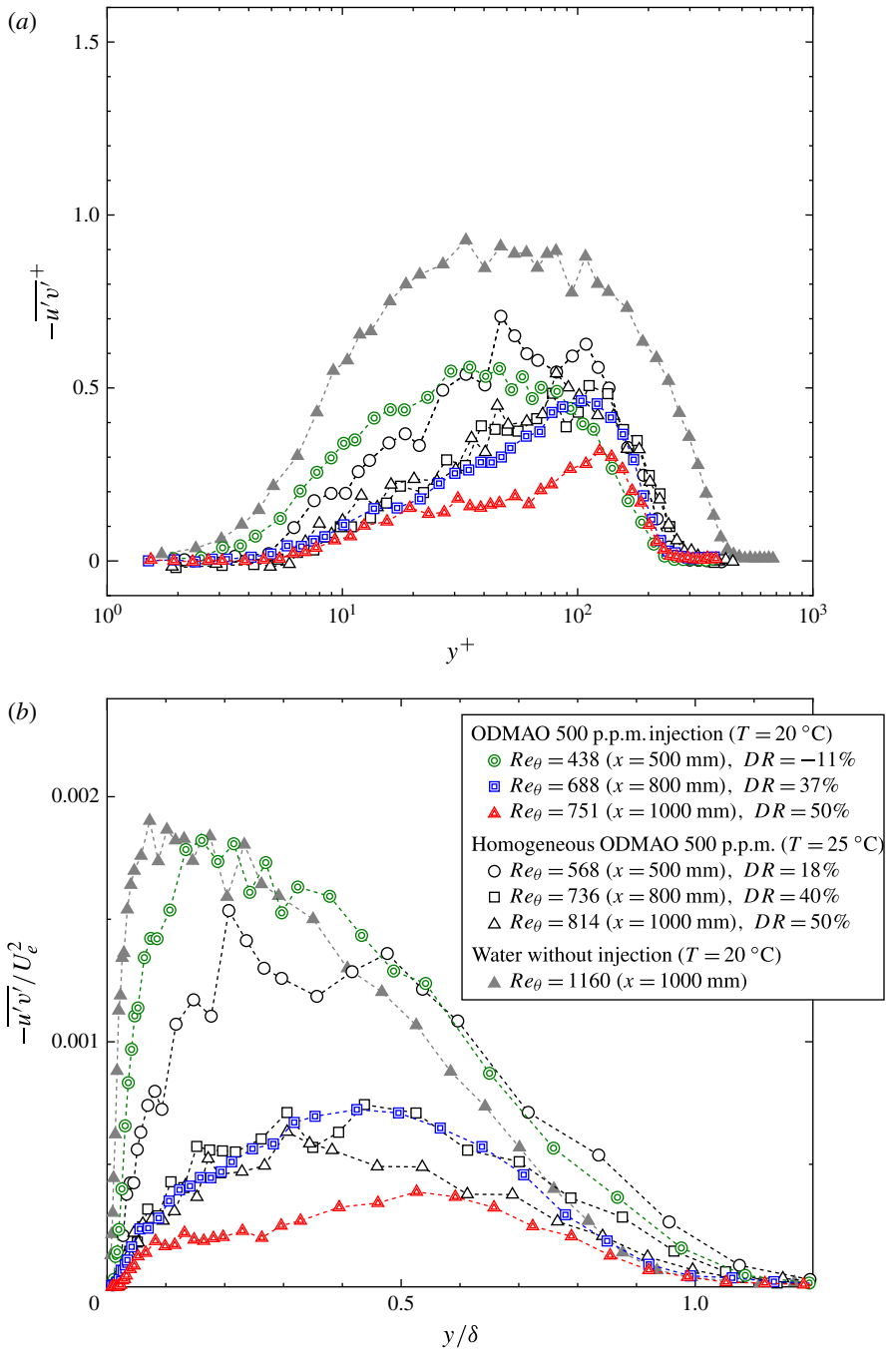


FIGURE 17. (Colour online) Reynolds shear stress profiles: (*a*) inner scaling; (*b*) outer scaling.

Mungal 2006). We cannot assume a nominally constant shear stress region near the wall for turbulent boundary layers of viscoelastic fluids, unlike Newtonian fluids. It is also difficult, however, to obtain the total shear stress for the turbulent boundary layer,

https://doi.org/10.1017/jfm.2014.225 Published online by Cambridge University Press

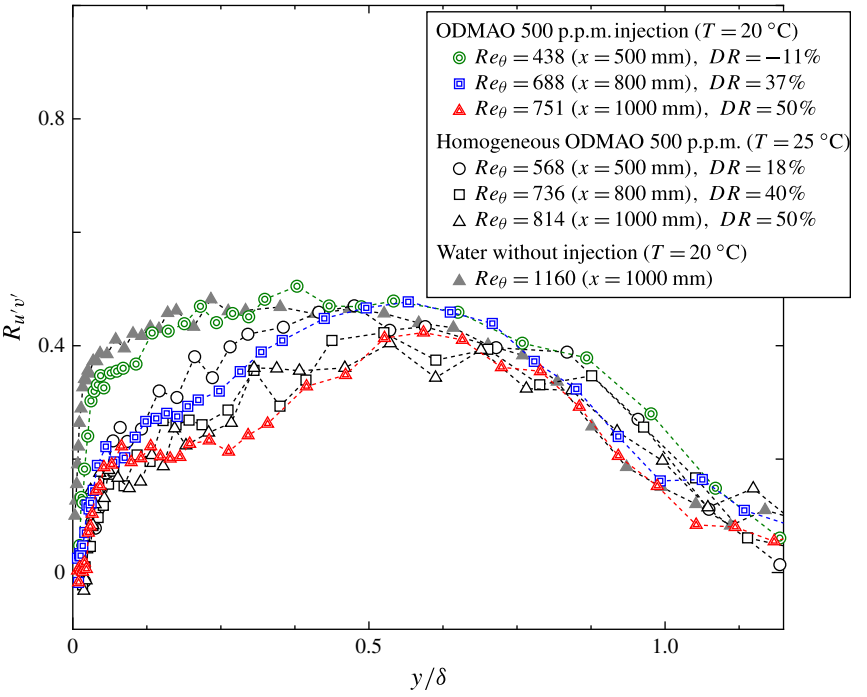


FIGURE 18. (Colour online) Correlation coefficient of streamwise and wall-normal fluctuation velocities profiles.

unlike the turbulent channel flow, in which the total shear stress or the wall shear stress is determined by the force balance with the pressure drop. Hou *et al.* (2006) proposed a new technique to determine total shear stress in a turbulent boundary layer with polymer additives. Their method is based on the $(1 - y/\delta)$ weighted straight-line fit.

Figure 19(*a*,*b*) shows profiles of $\mathrm{d}U^+/\mathrm{d}y^+ - \overline{u'v'}^+$ and $(1 - y/\delta)(\mathrm{d}U^+/\mathrm{d}y^+ - \overline{u'v'}^+)$ at $x = 1000$ mm. In figure 19(*b*), the dash-dotted line represents the relation for a Newtonian fluid at relatively low Reynolds numbers, $(1 - y/\delta)(\mathrm{d}U^+/\mathrm{d}y^+ - \overline{u'v'}^+) = -1.4y/\delta + 1$. It is confirmed that the $(1 - y/\delta)$ fit is reasonable for water at $x = 1000$ mm, which is consistent with the finding of Hou *et al.* (2006). For both injected surfactant and homogeneous surfactant solutions at $x = 1000$ mm, however, the weighted shear stress $(1 - y/\delta)(\mathrm{d}U^+/\mathrm{d}y^+ - \overline{u'v'}^+)$ is still smaller than that of water in the region $0.1 < y/\delta < 0.6$ as well as the shear stress $\mathrm{d}U^+/\mathrm{d}y^+ - \overline{u'v'}^+$. This is different from another finding of Hou *et al.* (2006) in which the values of $(1 - y/\delta)(\mathrm{d}U^+/\mathrm{d}y^+ - \overline{u'v'}^+)$ for polymer injection agree well with those for water in the region $0.2 < y/\delta < 0.5$. We confirmed the same trend at $x = 500$ and 800 mm (not shown here). The present results for the non-ionic surfactant solution are also consistent with our previous study on the drag-reducing turbulent boundary layer flow of homogeneous cationic surfactant solution (Tamano & Itoh 2011). The discrepancy between the present study and Hou *et al.* (2006) might be due to the difference in drag-reducing additives between the polymer and surfactant, but the reason still remains unknown. For further discussion about the total shear stress profile, the acquisition of additional experimental data on the streamwise variation in

https://doi.org/10.1017/jfm.2014.225 Published online by Cambridge University Press

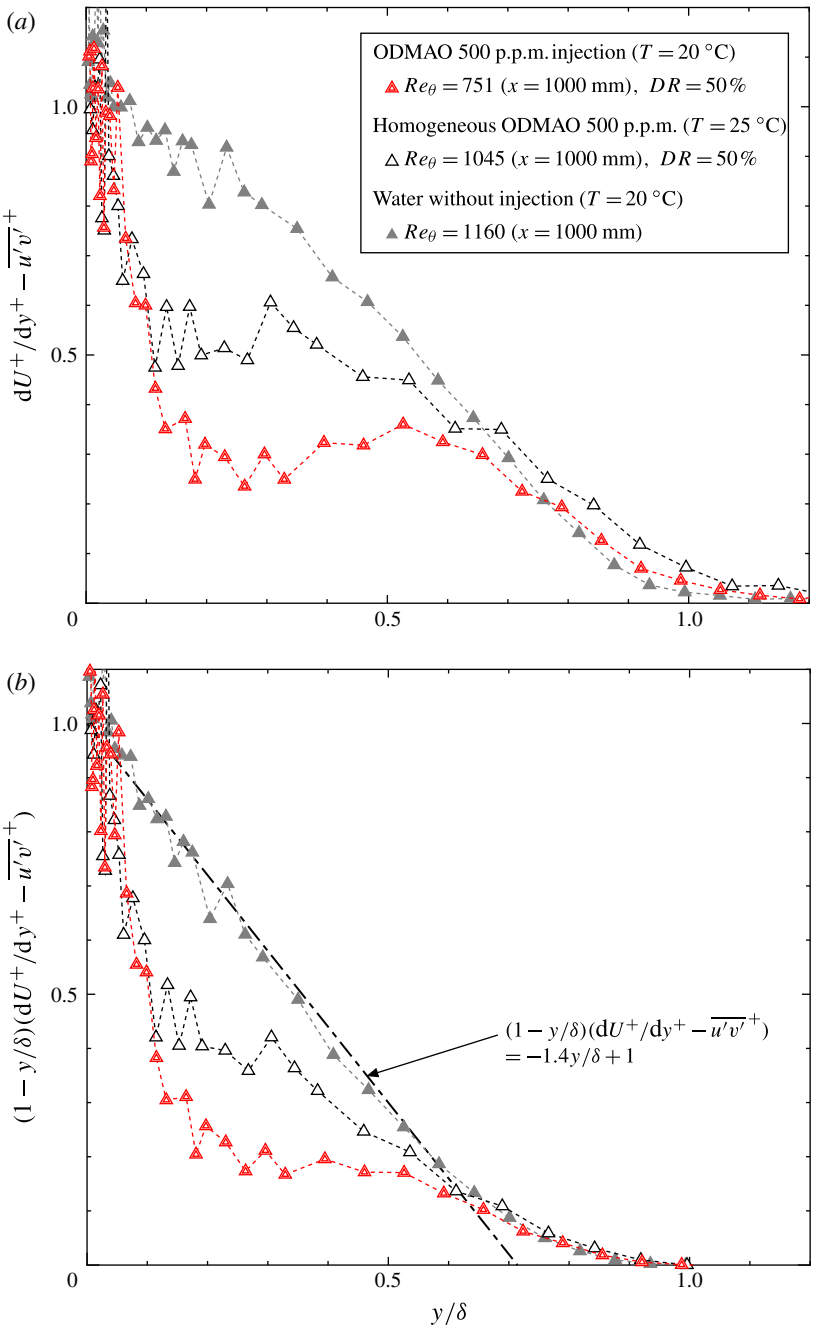


FIGURE 19. (Colour online) Shear stress profiles at $x = 1000$ mm: (*a*) $\mathrm{d}U^+/\mathrm{d}y^+ - \overline{u'v'}^+$; (*b*) $(1 - y/\delta)(\mathrm{d}U^+/\mathrm{d}y^+ - \overline{u'v'}^+)$.

the streamwise turbulence intensity, which could contribute to the total shear stress profile for the turbulent boundary layer flow, is needed especially at higher Reynolds number.

https://doi.org/10.1017/jfm.2014.225 Published online by Cambridge University Press

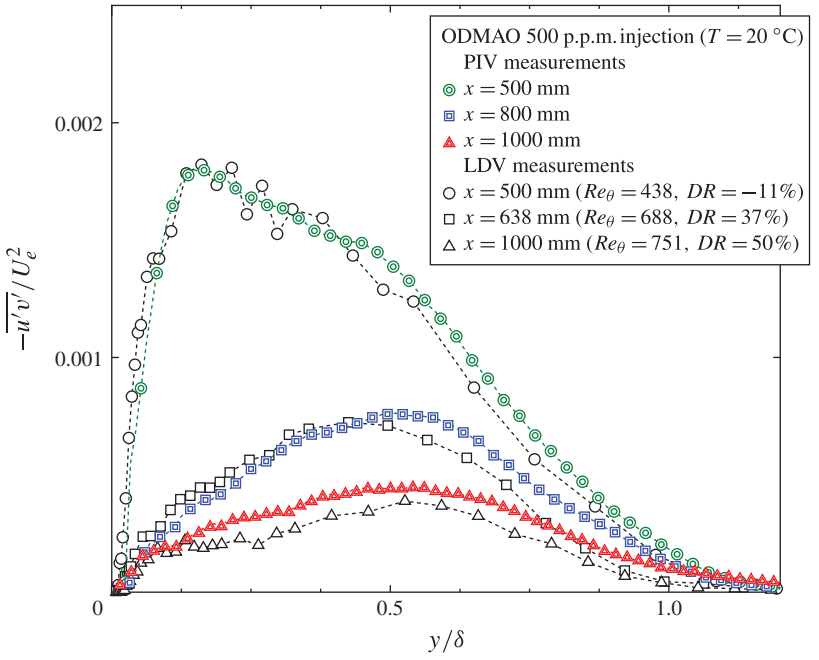


FIGURE 20. (Colour online) Comparison of Reynolds shear stress profiles with outer scaling between PIV and LDV measurements.

3.3. *Turbulence structures for surfactant injection*

To show the reliability of the present PIV measurements, the profiles of the Reynolds shear stress $-\overline{u'v'}/U_e^2$ are compared with the corresponding data obtained by the LDV measurement. Figure 20 shows that the profiles of the Reynolds shear stress for both water and surfactant injection obtained by PIV measurement agree well with the corresponding data obtained by LDV measurement. We also confirmed that the other turbulence statistics such as mean velocity and streamwise and wall-normal turbulence intensities obtained by PIV measurements agree well with those by LDV measurement, except in the region very close to the wall (not shown here). The comparison between PIV and LDV measurements demonstrates that the velocity fields obtained by the present PIV measurements are reliable for the discussion of turbulence structures below.

Figure 21(*a*,*b*) shows the typical fluctuating velocity vectors and contours of instantaneous streamwise velocity fluctuation u'/U_e on the streamwise and wall-normal (x–y) plane for water and the surfactant injection at $DR = 50\,\%$, respectively. In the figure, flow is from left to right, and the locations of $x'/\delta = 0$ and $y/\delta = 0$ correspond to those of $x = 1000$ mm and the wall, respectively. The vector represents the fluctuating velocity vector, in which the arrow scale is the same for both water and surfactant injection. For water, we can observe strong ejection events around $y/\delta = 0.5$ and several vortex cores near the wall and the edge of the turbulent boundary layer. We confirmed a self-sustaining mechanism of near-wall turbulence, which consists of ejection and sweep events and hairpin vortex packets (see e.g. Adrian, Meinhart & Tomkins 2000; Adrian 2007; Wallace 2013) by investigation of the time sequence of fluctuating velocity vector fields (not shown here), which was also consistent with the conceptual model presented by Robinson (1991). For surfactant injection, on the other

https://doi.org/10.1017/jfm.2014.225 Published online by Cambridge University Press

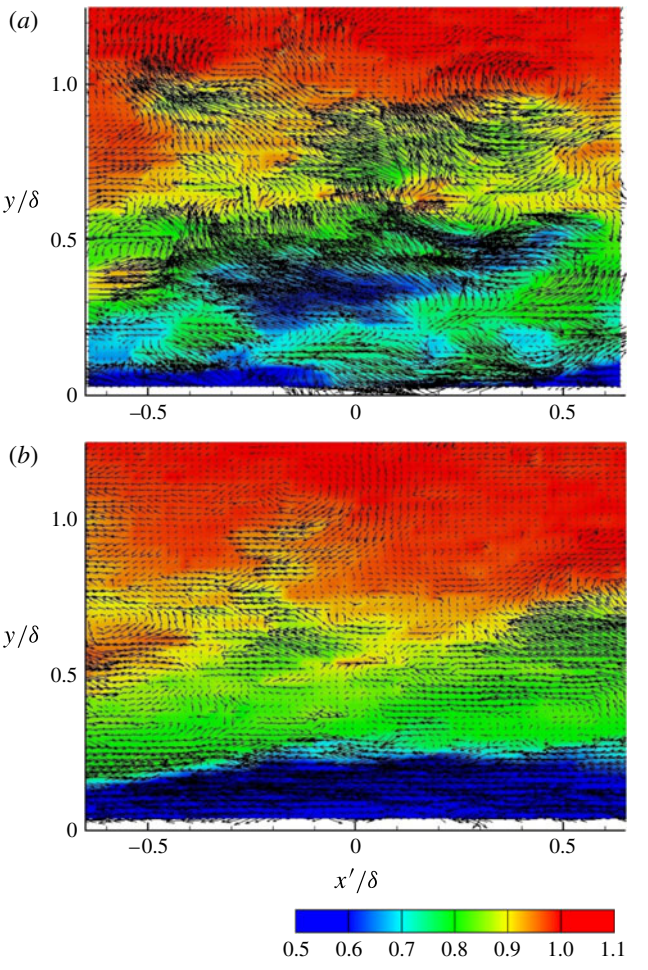


FIGURE 21. Fluctuation velocity vectors and contours of streamwise velocity U/U_e on the x–y plane around $x = 1000$ mm: (*a*) water without injection; (*b*) ODMAO 500 p.p.m. injection.

hand, the velocity fluctuations are attenuated across the turbulent boundary layer, and no clear vortex can be observed at this time. The fluctuating velocity vectors near the wall are almost parallel to the wall, which is consistent with the flow visualization (figure 5*b*) and the LDV measurements (figures 14 and 17), and almost the same as those of the homogeneous surfactant solutions (cf. Tamano *et al.* 2010).

Figure 22 shows the typical fluctuating velocity vectors on x–y around $x = 500$, 800 and 1000 mm for the surfactant injection. At $x = 500$ mm ($DR = -11\,\%$), strong sweep and ejection events are observed across the boundary layer, like for water. At $x = 800$ mm ($DR = 37\,\%$), there are some distinct vortical structures, which seem to be slightly elongated in the streamwise direction. At $x = 1000$ mm ($DR = 50\,\%$), the fluctuating velocity vectors close to the wall are almost parallel to the wall, and the wall-normal turbulent fluctuation is much smaller than those at $x = 500$ and 800 mm. These results support previous PIV findings (e.g. Warholic *et al.* 2001; Tamano *et al.* 2009*b*; Tamano *et al.* 2010).

https://doi.org/10.1017/jfm.2014.225 Published online by Cambridge University Press

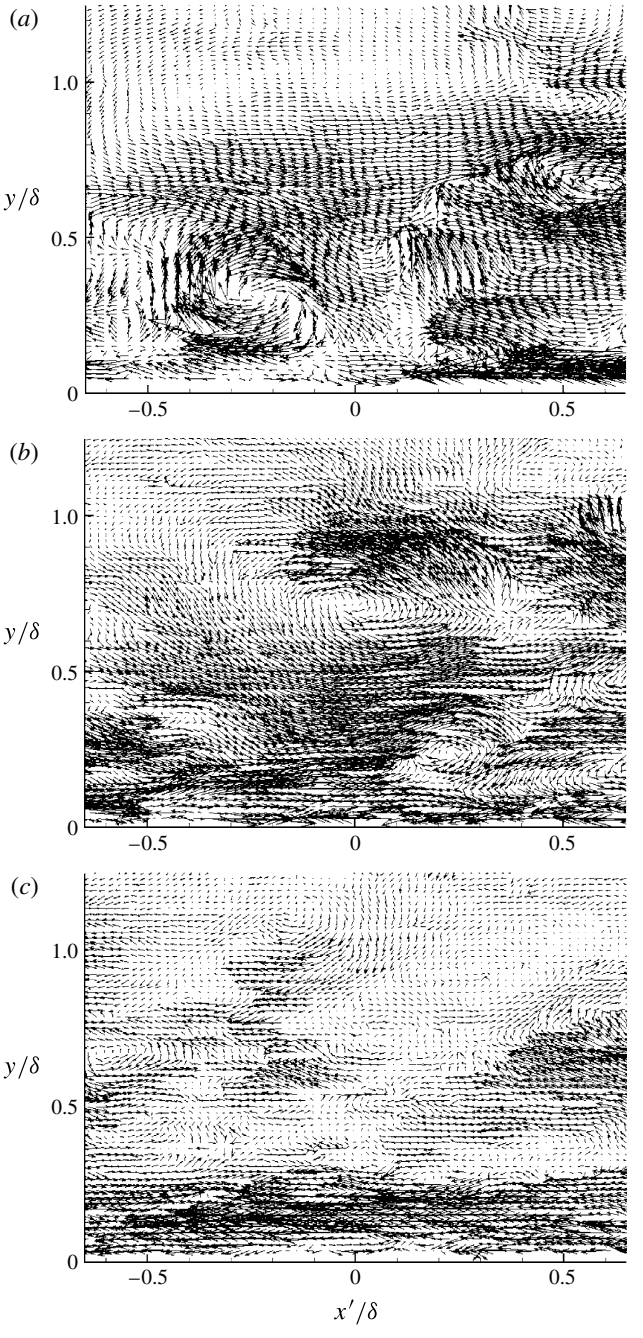


FIGURE 22. Fluctuation velocity vectors on the x–y plane with ODMAO 500 p.p.m. injection: (*a*) $x = 500$ mm; (*b*) $x = 800$ mm; (*c*) $x = 1000$ mm.

Figure 23 shows the fluctuating velocity vectors and contours of instantaneous streamwise velocity fluctuation u'/U_e in a wider region on the x–z plane at $y^+ \approx 40$ and around $x = 1000$ mm. The wall-normal locations of $y^+ \approx 40$ are based on the viscous length scale at $x'/\delta = 0$, in which the wall variables are obtained by LDV

https://doi.org/10.1017/jfm.2014.225 Published online by Cambridge University Press

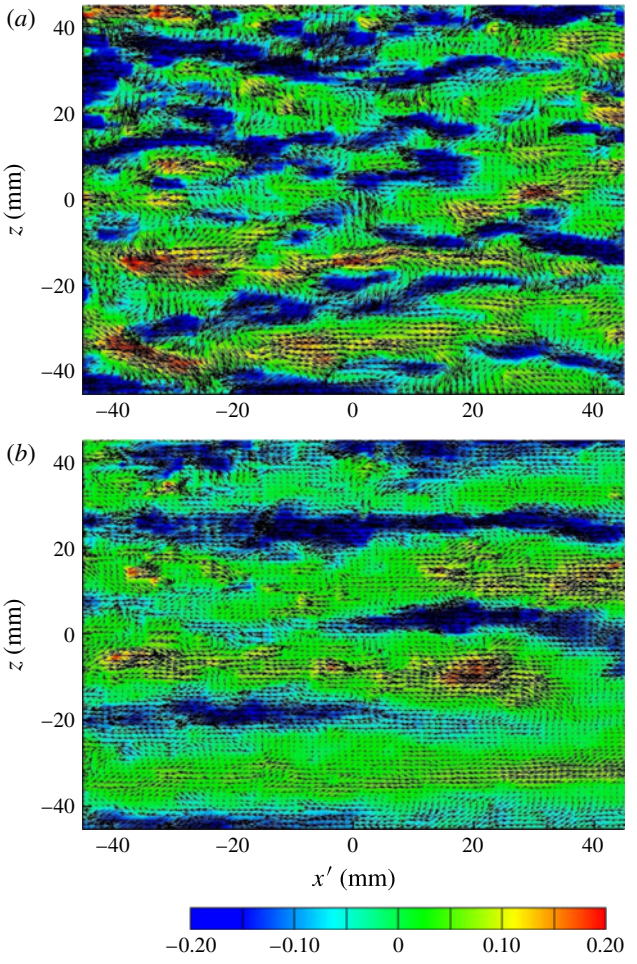


FIGURE 23. Fluctuation velocity vectors and contours of streamwise velocity fluctuation u'/U_e on the x–z plane at $y^+ \approx 40$ around $x = 1000$ mm: (a) water without injection; (b) ODMAO 500 p.p.m. injection.

measurement for water and surfactant injection. In this study, $y^+ \approx 40$ at $x = 1000$ mm corresponds to $y/\delta \simeq 0.08$ and 0.16 for water and surfactant injection, respectively. The high- and low-speed regions, which correspond to high- and low-speed streaks, are aligned laterally. Scales of high- and low-velocity regions (red and blue regions) for the surfactant injection are larger and their spanwise oscillation is strongly restricted, compared to water. The spanwise spacing of low-speed streaks seems to be enlarged, which is quantitatively discussed later. Compared with water, vortical structures for the surfactant injection are sparser and more elongated in the streamwise direction, and the spanwise fluctuation is much weaker.

Figure 24 shows the typical fluctuating velocity vectors on the x–z plane at $y^+ \simeq 40$ around $x = 500$, 800 and 1000 mm for surfactant injection. Several vortical structures, which seem to correspond to the cross-section of the legs of hairpin vortices (Robinson 1991; Tomkins & Adrian 2003), are observed at $x = 500$ mm. It is confirmed that regions of swirling strength with anticlockwise (clockwise) rotation

https://doi.org/10.1017/jfm.2014.225 Published online by Cambridge University Press

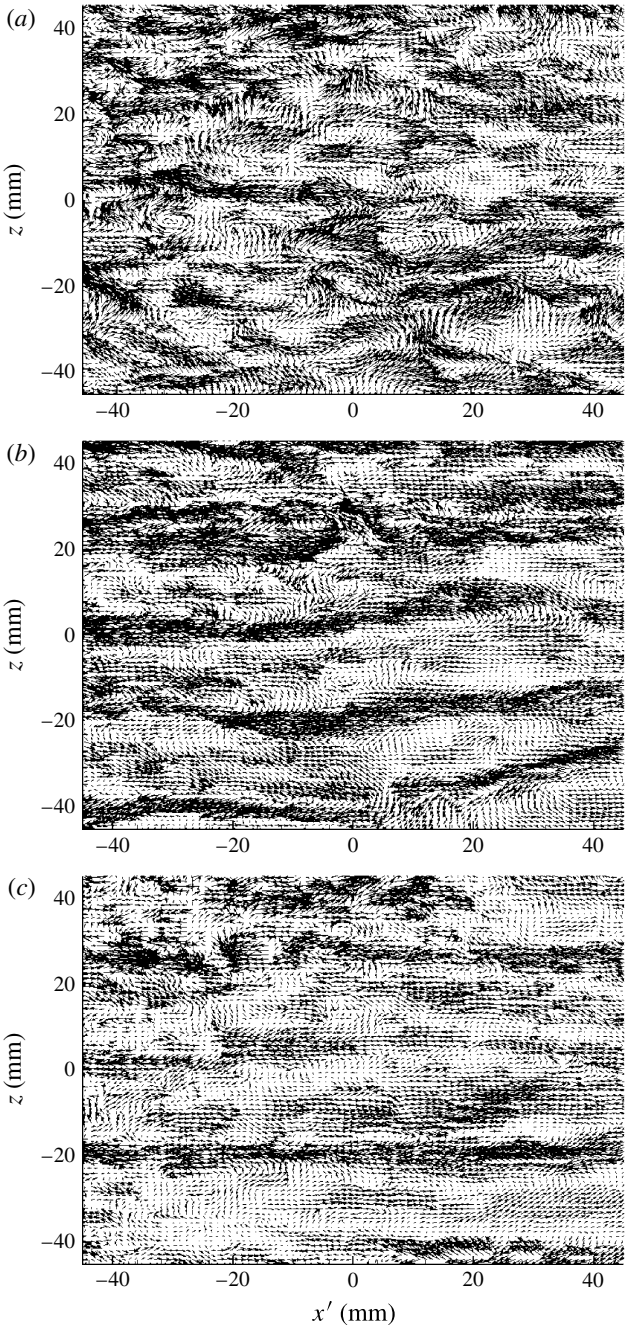


FIGURE 24. Fluctuation velocity vectors on the x–z plane at $y^+ \approx 40$ with ODMAO 500 p.p.m. injection: (*a*) $x = 500$ mm; (*b*) $x = 800$ mm; (*c*) $x = 1000$ mm.

tended to occur to the right (left) of the low-speed streaks, as pointed out by Tomkins & Adrian (2003). At $x = 800$ mm, vortical structures become sparser and some larger streaky structures are observed. At $x = 1000$ mm, the spanwise turbulence fluctuation is strongly suppressed and distinct vortical structures are hardly observed. Such

https://doi.org/10.1017/jfm.2014.225 Published online by Cambridge University Press

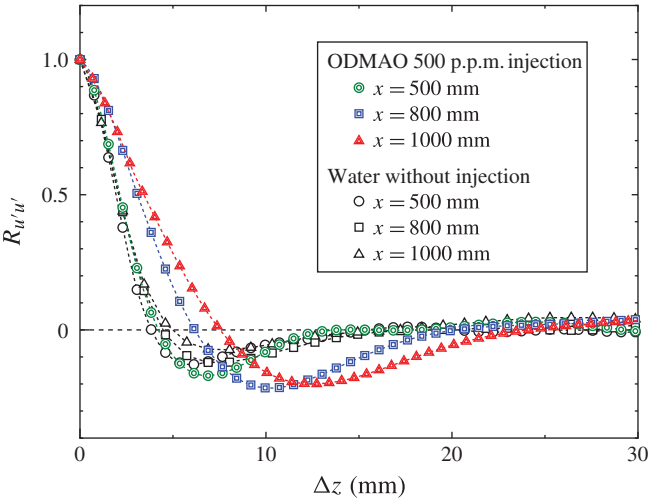


FIGURE 25. (Colour online) Profiles for two-point correlation of streamwise fluctuation velocities at $y^+ \approx 40$. The abscissa Δz is the spanwise spacing between two streamwise fluctuation velocities.

streamwise variation of turbulence structures on the x–z plane is consistent with that on the x–y plane (cf. figure 22).

Modification of low-speed streaks quantitatively, via the two-point correlation coefficient of streamwise velocity fluctuations, $R_{u'u'}$, which is a function of the spanwise spacing between two streamwise fluctuation velocities, Δz (figure 25), is then investigated. The spacing λ of the low-speed streaks corresponds to twice Δz at the minimum $R_{u'u'}$ (see e.g. Kim, Moin & Moser 1987). Figure 26 shows that the spanwise spacing of low-speed streaks for surfactant injection increases linearly with increase in x (i.e. *DR*) and is larger than that for water, which is consistent with results of the previous study on drag-reducing channel flows with polymer injection (e.g. Warholic *et al.* 2001) and turbulent boundary layers with polymer injection (e.g. White *et al.* 2004). Here, the value of λ is often scaled by the wall variables, and it is well known that the streak spacing in wall units λ^+, which is dependent on the wall-normal location and the Reynolds number, is around 100 for standard wall-bounded flows of Newtonian fluids (see e.g. Oldaker & Tiederman 1977). In this study, however, the abscissa Δz is plotted with dimensional scale, as well as in the PIV study of Warholic *et al.* (2001). This is because the PIV measurements here cannot directly provide the exact value of the local friction velocity as mentioned above. We confirmed that the spanwise spacing of low-speed streaks in wall units λ^+ for both water and surfactant injection, which was estimated by using the LDV measurements, was approximately 200 at different streamwise locations (i.e. *DR*), which is not consistent with previous studies (e.g. Oldaker & Tiederman 1977; White *et al.* 2004; Li *et al.* 2006*b*), in which λ^+ becomes larger with increase in drag reduction ratio. The present value of $\lambda^+ (\approx 200)$ for water is much larger than that for the standard wall-bounded turbulent flows of Newtonian fluids ($\lambda^+ \approx 100$). These discrepancies are mainly due to the fact that the wall-normal location of the x–z plane at $y^+ \approx 40$ is further away from the wall compared with the optimal wall-normal location for the discussion of low-speed streaks, i.e. $y^+ \approx 10$, owing to the limitation of the present PIV system.

https://doi.org/10.1017/jfm.2014.225 Published online by Cambridge University Press

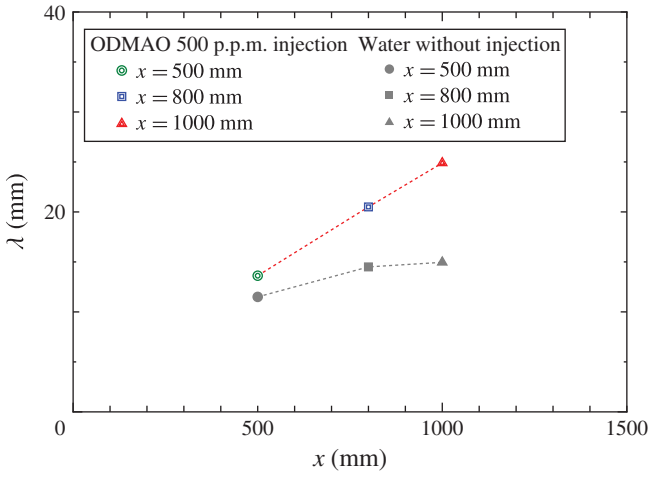


FIGURE 26. (Colour online) Streamwise variation in spanwise spacing of low-speed streaks at $y^+ \approx 40$.

To clarify the difference in turbulence structures, such as hairpin vortices and low-speed streaks, among water, surfactant injection and homogeneous surfactant solution, we present simple plausible pictures drawn by comprehensively considering the present results of the flow visualization, PLIF, LDV and PIV on the x–y and x–z planes and these time series images (not shown here), in addition to our previous experimental results for homogeneous non-ionic surfactant solutions (Tamano *et al.* 2010). Figure 27 is a schematic of conceptual models for the development of turbulence structures such as hairpin vortices and low-speed streaks for the turbulent boundary layer for a Newtonian fluid (water), the non-ionic surfactant (ODMAO 500 p.p.m.) injection and the homogeneous non-ionic surfactant (ODMAO 500 p.p.m.) solution. For water, there are several sharp hairpin vortices, which are drawn with reference to the schematic of the hairpin vortex attached to the wall (Adrian *et al.* 2000). Here, we do not take the case of the merging of vortex packets described in Tomkins & Adrian (2003). The several low-speed streaks are drawn almost between the legs of the hairpin vortex, and they are not the quasi-streamwise vortices that are the signature of the hairpin vortex (Adrian *et al.* 2000). The low-momentum region consisting of several low-speed streaks here would correspond to typical very long low-speed streaks, in which the length is approximately 2000–3000 viscous units (Adrian *et al.* 2000). At $x = 500$ mm, turbulence structures such as the hairpin vortex and low-speed streak for surfactant injection are similar to those for water, while the hairpin vortices for homogeneous surfactant solution are already elongated in the streamwise direction. In the region from $x = 800$ to 1000 mm, such turbulence structures for homogeneous surfactant solution and surfactant injection are quite similar to each other, in which both hairpin vortices with leg and head thicker and low-speed streaks with the spanwise width wider are elongated in the streamwise direction, i.e. with the increase in the drag reduction ratio, and their oscillating movement is strongly restricted in both wall-normal and spanwise directions. The inclination (growth) angle of vortex packets at $x = 1000$ mm is much smaller than that of water. It should be noted that these streamwise variations are also similar to the numerical study of Kim *et al.* (2008), in which the suppression of the autogeneration of new vortices and vortex packet formation was investigated for

https://doi.org/10.1017/jfm.2014.225 Published online by Cambridge University Press

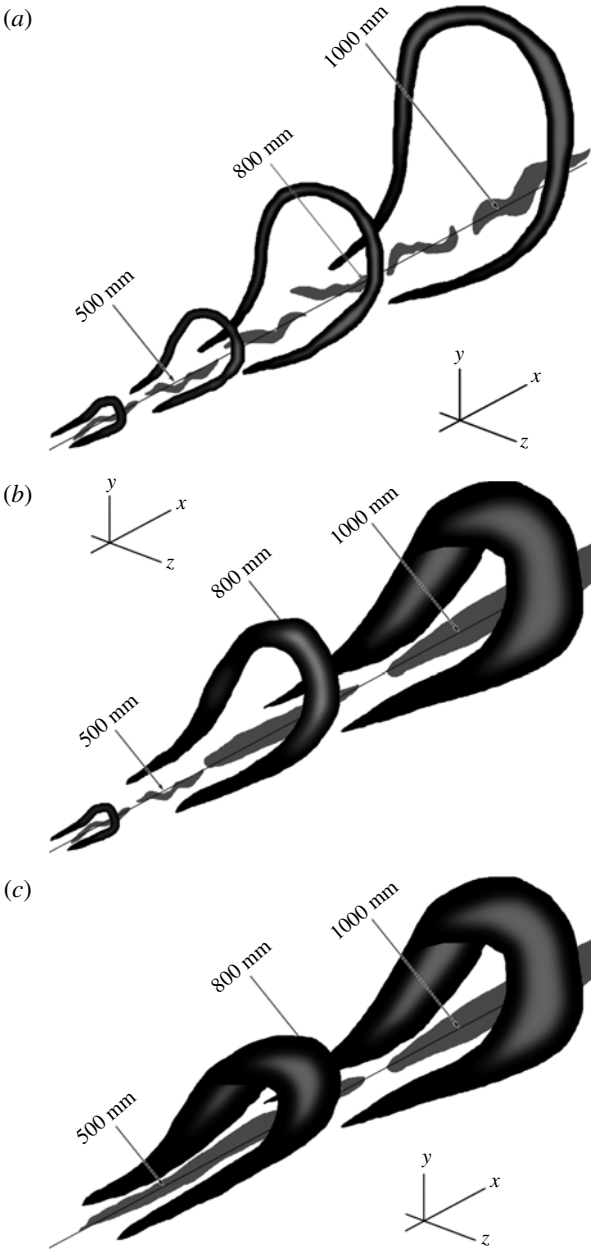


FIGURE 27. Schematics of conceptual models for development of hairpin vortices and low-speed streaks for turbulent boundary layer: (*a*) Newtonian fluid (water); (*b*) non-ionic surfactant (ODMAO 500 p.p.m.) injection; (*c*) homogeneous non-ionic surfactant (ODMAO 500 p.p.m.) solution.

a drag-reducing turbulent channel flow. The present physical models are applicable only for the present experiments, since the turbulence structures of a drag-reducing turbulent boundary layer are strongly dependent on the kinds of drag-reducing additives and their rheological properties in addition to the experimental conditions.

https://doi.org/10.1017/jfm.2014.225 Published online by Cambridge University Press

In particular, the difference in the kinds of drag reducers might result in essential differences in turbulence structures. Quite recently, Kulmatova, Bonn & Kellay (2013) reported that, even in the absence of wall effects, the structure of turbulence, i.e. the intermittency at small scales, was altered by the injection of cationic surfactant solutions with the shear-thickening property in a closed flow system, unlike the polymer solutions in which the reduction in the energy dissipation disappeared if the turbulence was forced completely inertially (see Cadot, Bonn & Douady 1998). However, the conceptual models here would be helpful for clearly understanding the difference in the development of near-wall turbulence structures between homogeneous and heterogeneous non-ionic surfactant solutions, and then the related drag-reducing mechanism.

4. Conclusions

The drag reduction of turbulent boundary layer flow with the injection of non-ionic surfactant solutions was investigated by the flow visualization measurements, PLIF measurements, two-component LDV measurements and PIV measurements on the streamwise and wall-normal (x–y) plane and the streamwise and spanwise (x–z) plane. We focus on the development of turbulence statistics between premixed (homogeneous) and injected (heterogeneous) surfactant solutions, which is the first attempt at a drag-reducing turbulent boundary layer, as far as we know. For both cases of homogeneous and heterogeneous surfactant solutions, in which the concentration of surfactant solution is the same ($C = 500$ p.p.m.) but the temperature and degree of degradation are different, the drag reduction ratios DR increase in the streamwise direction and are the same ($DR = 50\,\%$) at $x = 1000$ mm, where PLIF measurements show that the injected surfactant solution is still in the process of diffusion and the local concentration is slightly lower than that for the homogeneous surfactant solution. LDV measurements showed that the development of the turbulent boundary layer parameters, such as the friction coefficient and shape factor, are essentially similar for both cases. It can be concluded that the surfactant injection method is more effective in obtaining the drag reduction effect for the turbulent boundary layer than the homogeneous surfactant method, which needs a much greater amount of surfactant additives, if one does not take into account the power needed for moving the piston for the surfactant injection.

For both surfactant injection and homogeneous surfactant cases, turbulence statistics with outer and inner scaling showed the behaviour of typical drag-reducing flow such as the shift up in the log law region for the mean velocity in wall units and the decrease in the wall-normal turbulence intensity and the Reynolds shear stress. The streamwise variation in the mean velocity in wall units is well correlated with that of the drag reduction ratio. It is found that the largest difference in the streamwise variations in the maxima of streamwise turbulence intensity is between heterogeneous and homogeneous surfactant solutions. It can be concluded that the behaviour of streamwise turbulence intensity is strongly dependent on both how the boundary layer develops and how to normalize it, which may be due to the formation of layered (or sheet-like) structures parallel to the wall. This finding supports the previous studies in which the behaviour of streamwise turbulence intensity is very complex for polymer (White & Mungal 2008) and cationic surfactant (Tamano *et al.* 2009*b*) additives. The wall-normal locations of streamwise and wall-normal turbulence intensities are gradually away from the wall with increase in the streamwise location, whose variations correspond well to that of the drag reduction ratio. It is also

https://doi.org/10.1017/jfm.2014.225 Published online by Cambridge University Press

revealed that the drag reduction ratio is closely correlated not with the Reynolds shear stresses scaled by outer and inner variables but with the correlation coefficient of the streamwise and wall-normal turbulent fluctuations. The technique of Hou *et al.* (2006, 2008) to determine total shear stress in a turbulent boundary layer with polymer additives is not applicable to the present study for surfactant additives, in which the LDV measurement is used to determine the wall-shear stress. In order to extend the range of application for the fitting method of Hou *et al.* (2006, 2008) to the surfactant injection case, in which the streamwise variation in the streamwise turbulence intensity is quite complex, a further improvement would be desired, so that the turbulence statistics with inner scaling could be obtained only by PIV measurements.

The PIV measurements on the streamwise and wall-normal plane and the streamwise and spanwise plane revealed that, as well as the case of the non-ionic homogeneous surfactant solution (Tamano *et al.* 2010), turbulence structures such as hairpin vortices and low-speed streaks with the injection of the non-ionic surfactant solution were more suppressed and modified in the streamwise direction, so that layered (sheet-like) structures parallel to the wall were formed in the near-wall region, which was consistent with the previous studies on the turbulent boundary layer with polymer additives (Hou *et al.* 2008). The difference in turbulence structures among water (Newtonian), surfactant injection and homogeneous surfactant was pictured by a simple conceptual model, which would be now of narrow application due to the unknown rheological properties of the surfactant solutions used here and the small range of Reynolds number. Nevertheless, the present experimental data can be expected to be used for constructing the new constitutive equation models for the DNS (see Dimitropoulos *et al.* 2006), which could capture the new physics of drag reduction of a turbulent boundary layer with the injection of aqueous surfactant or polymer solution.

Acknowledgements

We are grateful to Professor M. Itoh of Aichi University of Technology for his valuable suggestions. We are also indebted to Mr Y. Matsuno, Mr J. Ito and Mr K. Nishio for their generous assistance with the experimental measurements. This work was supported by a Grant-in-Aid for Scientific Research (nos 21760126 and 23686029) from the Japan Society for the Promotion of Science. Special thanks are also due Lion Akzo Co. Ltd for providing the non-ionic surfactant solutions.

REFERENCES

ADRIAN, R. J. 2007 Hairpin vortex organization in wall turbulence. *Phys. Fluids* **19**, 041301.

ADRIAN, R. J., MEINHART, C. D. & TOMKINS, C. D. 2000 Vortex organization in the outer region of the turbulent boundary layer. *J. Fluid Mech.* **422**, 1–54.

AGUILAR, G., GASLJEVIC, K. & MATTHYS, E. F. 2001 Asymptotes of maximum friction and heat transfer reductions for drag-reducing surfactant solutions. *Intl J. Heat Mass Transfer* **44**, 2835–2843.

BONN, D., AMAROUCHENE, Y., WAGNER, C., DOUADY, S. & CADOT, O. 2005 Turbulent drag reduction by polymers. *J. Phys.: Condens. Matter* **17**, S1195–S1202.

BRONIARZ-PRESS, L., ROZANSKI, J. & ROZANSKA, S. 2007 Drag reduction effect in pipe systems and liquid falling film flow. *Rev. Chem. Engng* **23**, 149–245.

CADOT, O., BONN, D. & DOUADY, S. 1998 Turbulent drag reduction in a closed flow system: boundary layer versus bulk effects. *Phys. Fluids* **10**, 426–436.

https://doi.org/10.1017/jfm.2014.225 Published online by Cambridge University Press

CAI, S. P., SUZUKI, H. & KOMODA, Y. 2012 Drag-reduction of a nonionic surfactant aqueous solution and its rheological characteristics. *Sci. China Technol. Sci.* **55**, 772–778.

COLES, D. E. 1962 A manual of experimental boundary-layer practice for low-speed flow. *Rand Rep.* No. R-403-PR. The Rand Corp., Santa Monica, CA.

DIMITROPOULOS, C. D., DUBIEF, Y., SHAQFEH, E. S. G. & MOIN, P. 2006 Direct numerical simulation of polymer-induced drag reduction in turbulent boundary layer flow of inhomogeneous polymer solutions. *J. Fluid Mech.* **566**, 153–162.

DIMITROPOULOS, C. D., DUBIEF, Y., SHAQFEH, E. S. G., MOIN, P. & LELE, S. K. 2005 Direct numerical simulation of polymer-induced drag reduction in turbulent boundary layer flow. *Phys. Fluids* **17**, 011705.

DIMITROPOULOS, C. D., SURESHKUMAR, R. & BERIS, A. N. 1998 Direct numerical simulation of viscoelastic turbulent channel flow exhibiting drag reduction: effect of the variation of rheological parameters. *J. Non-Newtonian Fluid Mech.* **79**, 433–468.

DRAPPIER, J., DIVOUX, T., AMAROUCHENE, Y., BERTRAND, F., RODTS, S., CADOT, O., MEUNIER, J. & BONN, D. 2006 Turbulent drag reduction by surfactants. *Europhys. Lett.* **74**, 362–368.

DUBIEF, Y., TERRAPON, V. E. & SORIA, J. 2013 On the mechanism of elasto-inertial turbulence. *Phys. Fluids* **25**, 110817.

ELBING, B. R., PERLIN, M., DOWLING, D. R. & CECCIO, S. L. 2013 Modification of the mean near-wall velocity profile of a high-Reynolds number turbulent boundary layer with the injection of drag-reducing polymer solutions. *Phys. Fluids* **25**, 085103.

ELBING, B. R., SOLOMON, M. J., PERLIN, M., DOWLING, D. R. & CECCIO, S. L. 2011 Flow-induced degradation of drag-reducing polymer solutions within a high Reynolds number turbulent boundary layer. *J. Fluid Mech.* **670**, 337–364.

ESCUDIER, M. P., PRESTI, F. & SMITH, S. 1999 Drag reduction in the turbulent pipe flow of polymers. *J. Non-Newtonian Fluid Mech.* **81**, 197–213.

FONTAINE, A. A., PETRIE, H. L. & BRUNGART, T. A. 1992 Velocity profile statistics in turbulent boundary layer with slot-injected polymer. *J. Fluid Mech.* **238**, 435–466.

FRINGS, B. 1988 Heterogeneous drag reduction in turbulent pipe flows using various injection techniques. *Rheol. Acta* **27**, 92–110.

GASLJEVIC, K., AGUILAR, G. & MATTHYS, E. F. 2001 On two distinct types of drag-reducing fluids, diameter scaling, and turbulent profiles. *J. Non-Newtonian Fluid Mech.* **96**, 405–425.

GASLJEVIC, K., HOYER, K. & MATTHYS, E. F. 2007 Temporary degradation and recovery of drag-reducing surfactant solutions. *J. Rheol.* **51**, 645–667.

GYR, A. & BEWERSDORFF, H.-W. 1995 *Drag Reduction of Turbulent Flows by Additives*. Kluwer Academic.

HOU, Y., SOMANDEPALLI, V. S. R. & MUNGAL, M. G. 2006 A technique to determine total shear stress and polymer stress profiles in drag reduced boundary layer flows. *Exp. Fluids* **40**, 589–600.

HOU, Y., SOMANDEPALLI, V. S. R. & MUNGAL, M. G. 2008 Streamwise development of turbulent boundary-layer drag reduction with polymer injection. *J. Fluid Mech.* **597**, 31–66.

HOUSIADAS, K. D. & BERIS, A. N. 2004 An efficient fully implicit spectral scheme for DNS of turbulent viscoelastic channel flow. *J. Non-Newtonian Fluid Mech.* **122**, 243–262.

HOYT, J. W. & SELLIN, R. H. J. 1991 Polymer threads and drag reduction. *Rheol. Acta* **30**, 307–315.

HU, Y. & MATTHYS, E. F. 1997 Rheological and rheo-optical characterization of shear-induced structure formation in a nonionic drag-reducing surfactant solution. *J. Rheol.* **41**, 151–166.

ITOH, M., TAMANO, S., YOKOTA, K. & NINAGAWA, M. 2005 Velocity measurement in turbulent boundary layer of drag-reducing surfactant solution. *Phys. Fluids* **17**, 075107.

KIM, K., ADRIAN, R. J., BALACHANDAR, S. & SURESHKUMAR, R. 2008 Dynamics of hairpin vortices and polymer-induced turbulent drag reduction. *Phys. Rev. Lett.* **100**, 134504.

KIM, J., MOIN, P. & MOSER, R. 1987 Turbulence statistics in fully developed channel flow at low Reynolds number. *J. Fluid Mech.* **177**, 133–166.

KOSKIE, J. E. & TIEDERMAN, W. G. 1991 Polymer drag reduction of a zero-pressure-gradient boundary layer. *Phys. Fluids* A **3**, 2471–2473.

https://doi.org/10.1017/jfm.2014.225 Published online by Cambridge University Press

KULMATOVA, D., BONN, D. & KELLAY, H. 2013 High-Reynolds-number turbulence in complex fluids. *Europhys. Lett.* **101**, 24002.

LI, C.-F., SURESHKUMAR, R. & KHOMAMI, B. 2006*a* Influence of rheological parameters on polymer induced turbulent drag reduction. *J. Non-Newtonian Fluid Mech.* **140**, 23–40.

LI, F.-C., KAWAGUCHI, Y., HISHIDA, K. & OSHIMA, M. 2006*b* Investigation of turbulence structures in a drag-reduced turbulent channel flow with surfactant additive by stereoscopic particle image velocimetry. *Exp. Fluids* **40**, 218–230.

LI, F.-C., YU, B., WEI, J.-J. & KAWAGUCHI, Y. 2012 *Turbulent Drag Reduction by Surfactant Additives*. John Wiley & Sons.

LIN, Z., ZHENG, Y., DAVIS, H. T., SCRIVEN, L. E., TALMON, Y. & ZAKIN, J. L. 2000 Unusual effects of counterion to surfactant concentration ratio on viscoelasticity of a cationic surfactant drag reducer. *J. Non-Newtonian Fluid Mech.* **93**, 363–373.

LU, B., LI, X., SCRIVEN, L. E., DAVIS, H. T., TALMON, Y. & ZAKIN, J. L. 1998*a* Effect of chemical structure on viscoelasticity and extensional viscosity of drag-reducing cationic surfactant solutions. *Langmuir* **14**, 8–16.

LU, B., ZHENG, Y., DAVIS, H. T., SCRIVEN, L. E., TALMON, Y. & ZAKIN, J. L. 1998*b* Effect of variations in counterion to surfactant ratio on rheology and microstructures of drag reducing cationic surfactant systems. *Rheol. Acta* **37**, 528–548.

OLDAKER, D. J. & TIEDERMAN, W. G. 1977 Spatial structure of the viscous sublayer in drag-reducing channel flows. *Phys. Fluids* **20**, S133–S144.

QI, Y. & ZAKIN, J. L. 2002 Chemical and rheological characterization of drag-reducing cationic surfactant systems. *Ind. Engng Chem. Res.* **41**, 6326–6336.

ROBINSON, S. K. 1991 Coherent motions in the turbulent boundary layer. *Annu. Rev. Fluid Mech.* **23**, 601–639.

SAMANTA, D., DUBIEF, Y., HOLZNER, M., SCHÄFER, C., MOROZOV, A. N., WAGNER, C. & HOF, B. 2013 Elasto-inertial turbulence. *Proc. Natl Acad. Sci. USA* **110**, 10 557–10 562.

SOMANDEPALLI, V. S. R., HOU, Y. X. & MUNGAL, M. G. 2010 Concentration flux measurements in a polymer drag-reduced turbulent boundary layer. *J. Fluid Mech.* **644**, 281–319.

SUN CHEE FORE, R., SZWALEK, J. & SIRVIENTE, A. I. 2005 The effects of polymer solution preparation and injection on drag reduction. *J. Fluids Engng* **127**, 536–549.

TAMANO, S., GRAHAM, M. D. & MORINISHI, Y. 2011 Streamwise variation of turbulent dynamics in boundary layer flow of drag-reducing fluid. *J. Fluid Mech.* **686**, 352–377.

TAMANO, S. & ITOH, M. 2011 Comparison of turbulence structures at large and small drag reduction ratios in turbulent boundary layer of surfactant solutions. *J. Turbul.* **12** (18), 1–22.

TAMANO, S., ITOH, M., HOSHIZAKI, K. & YOKOTA, K. 2007 Direct numerical simulation on the drag-reducing turbulent boundary layer of viscoelastic fluid. *Phys. Fluids* **19**, 075106.

TAMANO, S., ITOH, M., HOTTA, S., YOKOTA, K. & MORINISHI, Y. 2009*a* Effect of rheological properties on drag reduction in turbulent boundary layer flow. *Phys. Fluids* **21**, 055101.

TAMANO, S., ITOH, M., INOUE, T., KATO, K. & YOKOTA, K. 2009*b* Turbulence statistics and structures of drag-reducing turbulent boundary layer in homogeneous aqueous surfactant solutions. *Phys. Fluids* **21**, 045101.

TAMANO, S., ITOH, M., KATO, K. & YOKOTA, K. 2010 Turbulent drag reduction in nonionic surfactant solutions. *Phys. Fluids* **22**, 055102.

TAMANO, S., MIYAGAWA, K., MORINISHI, Y., ITOH, M. & TAGA, K. 2012 Effects of degradation on drag reduction in turbulent pipe flow of nonionic surfactant aqueous solutions. *Nihon Reoroji Gakkaishi* **40**, 69–77.

TIEDERMAN, W. G., LUCHIK, T. S. & BOGARD, D. G. 1985 Wall-layer structure and drag reduction. *J. Fluid Mech.* **156**, 419–437.

TOMKINS, C. D. & ADRIAN, R. J. 2003 Spanwise structure and scale growth in turbulent boundary layers. *J. Fluid Mech.* **490**, 37–74.

VIRK, P. S. 1975 Drag reduction fundamentals. *AIChE J.* **21** (4), 625–656.

VLEGGAAR, J. & TELS, M. 1973 Drag reduction by polymer threads. *Chem. Engng Sci.* **28**, 965–968.

WAGNER, C., AMAROUCHENE, Y., DOYLE, P. & BONN, D. 2006 Turbulent-drag reduction of polyelectrolyte solutions: relation with the elongational viscosity. *Europhys. Lett.* **64**, 823–829.

https://doi.org/10.1017/jfm.2014.225 Published online by Cambridge University Press

WALLACE, J. M. 2013 Highlights from 50 years of turbulent boundary layer research. *J. Turbul.* **13** (53), 1–70.

WARHOLIC, M. D., HEIST, D. K., KATCHER, M. & HANRATTY, T. J. 2001 A study with particle-image velocimetry of the influence of drag-reducing polymers on the structure of turbulence. *Exp. Fluids* **31**, 474–483.

WARHOLIC, M. D., SCHMIDT, G. M. & HANRATTY, T. J. 1999 The influence of a drag-reducing surfactant on a turbulent velocity field. *J. Fluid Mech.* **388**, 1–20.

WHITE, C. M., DUBIEF, Y. & KLEWICKI, J. 2012 Re-examining the logarithmic dependence of the mean velocity distribution in polymer drag reduced wall-bounded flow. *Phys. Fluids* **24**, 021701.

WHITE, C. M. & MUNGAL, M. G. 2008 Mechanics and prediction of turbulent drag reduction with polymer additives. *Annu. Rev. Fluid Mech.* **40**, 235–256.

WHITE, C. M., SOMANDEPALLI, V. S. R. & MUNGAL, M. G. 2004 The turbulence structure of drag-reduced boundary layer flow. *Exp. Fluids* **36**, 62–69.

WINKEL, E. S., OWEIS, G., VANAPALLI, S. A., DOWLING, D. R., PERLIN, M., SOLOMON, M. J. & CECCIO, S. L. 2009 High Reynolds number turbulent boundary layer friction drag reduction from wall-injected polymer solutions. *J. Fluid Mech.* **621**, 259–288.

WU, J. & TULIN, M. P. 1972 Drag reduction by ejecting additive solutions into a pure water boundary layer. *Trans. ASME* D: *J. Basic Engng* **94**, 749–755.

ZAKIN, J. L. & GE, W. 2010 Polymer and surfactant drag reduction in turbulent flows. In *Polymer Physics: From Suspensions to Nanocomposites and Beyond* (ed. L. A. Utracki & A. M. Jamieson), pp. 89–127. John Wiley & Sons.

ZAKIN, J. L., LU, B. & BEWERSDORFF, H.-W. 1998 Surfactant drag reduction. *Rev. Chem. Engng* **14**, 253–318.

https://doi.org/10.1017/jfm.2014.225 Published online by Cambridge University Press